1

Energetics and Mechanisms for Decomposition of Cationized Amino Acids and Peptides Explored Using Guided Ion Beam Tandem Mass Spectrometry

P. B. Armentrout

315 S 1400 E Rm 2020, Department of Chemistry, University of Utah, Salt Lake City, UT 84112, USA

email: armentrout@chem.utah.edu; (801) 581-7885

Short title: Cationized amino acid and peptide decomposition

Keywords: ab initio calculations, deamidation, dehydration, statistical theory, thermochemistry, transition states

2

Biographical sketch

Peter B. Armentrout, Department of Chemistry, University of Utah, Utah, USA

Some 40 years ago, Professor Armentrout and his group developed the first guided ion beam tandem mass spectrometer to quantitatively examine the kinetic energy dependence of ion—molecule reactions. In the interim, he and his group have developed sophisticated tools for analyzing the resultant reaction cross sections and thereby providing thermodynamic, kinetic, and dynamic information on a wide range of chemical species. Innovative use of a variety of ion sources has extended the applicability of these methods to a host of interesting inorganic and biological molecules. His group is well-known for providing quality thermodynamic information for species ranging from diatomic molecules, to atomic clusters, to solvated systems, and biopolymers. Professor Armentrout has been a faculty member in the Department of Chemistry at the University of Utah since 1987. He has been recognized by a number of awards and his research is documented in over 535 refereed articles and book chapters.

ACRONYMS:

6P – hexapole ion guide

A - Ala - alanine

AA - amino acid

AMOx – 2-aminomethyl-5-oxazolone

Asn – asparagine

CAD – collisionally activated dissociation

CID – collision-induced dissociation

C - Cys - cysteine

DKP - diketopiperazine

ESI – electrospray ionization

EM – energized molecule

FELIX - Free Electron Lasers for Infrared eXperiments

FTICR – Fourier transform ion cyclotron resonance

FWHM – full width at half maximum

G - Gly - glycine

GG - Glygly - diglycine

GGG - Glyglygly - triglycine

GIBMS – guided ion beam tandem mass spectrometry

 $GS-ground\ structure$

IF – ion funnel

IRMPD – infrared multiple photon dissociation

MB-Maxwell-Boltzmann

MS – mass spectrometry

P - Pro - proline

PA – proton affinity

PSL – phase space limit

QMF – quadrupole mass filter

rf – radio frequency

SORI – sustained off-resonance irradiation

TCID - threshold collision-induced dissociation

TTS – tight transition state

Table of Contents

- 1 Introduction
- 2 Experimental Approach
 - 2.1 General
 - 2.2 Types of Reactions
 - 2.3 Data Modeling
 - 2.4 Computational Details
- 3 Alkali Metal Cationized Amino Acids and Glycine Biopolymers
 - 3.1 Lithiated Amino Acids
 - 3.2 Sodiated and Potassiated Amino Acids
 - 3.3 Sodiated and Potassiated Diglycine and Triglycine
- 4 Protonated Amino Acids
 - 4.1 Protonated Glycine
 - 4.2 Protonated Cysteine
 - 4.3 Protonated Asparagine
- 5 Protonated Glycine Biopolymers and Related Species
 - 5.1 Protonated Diglycine
 - 5.2 Protonated Triglycine
 - 5.3 Protonated GlyAlaGly
 - 5.4 Protonated GlyGlyAla
 - 5.5 Protonated GlyProAla
 - 5.6 Thermodynamic Overview
- 6 Protonated Dipeptides Containing Asparagine
 - 6.1 Overview
 - 6.2 Protonated AsnGly
 - 6.3 Protonated AsnAla and AsnVal
 - 6.4 Protonated AsnSer and AsnThr
 - 6.5 Thermodynamic Overview
- 7 Conclusions

Abstract

Fragmentation studies of cationized amino acids and small peptides as studied using guided ion beam tandem mass spectrometry (GIBMS) are reviewed. After a brief examination of the key attributes of the GIBMS approach, results for a variety of systems are examined, compared, and contrasted. Cationization of amino acids, diglycine, and triglycine with alkali cations generally leads to dissociations in which the intact biomolecule is lost. Exceptions include most lithiated species as well as a few examples for sodiated and one example for potassiated species. Like the lithiated species, cationization by protons leads to numerous dissociation channels. Results for protonated glycine, cysteine, asparagine, diglycine, and a series of tripeptides are reviewed, along with the thermodynamic consequences that can be gleaned. Finally, the important physiological process of the deamidation of asparagine (Asn) residues is explored by the comparison of five dipeptides in which the C-terminal partner (AsnXxx) is altered. The GIBMS thermochemistry is shown to correlate well with kinetic results from solution phase studies.

1 INTRODUCTION

In 2011, Vekey and co-workers published an article in Mass Spectrometry Reviews entitled "Leucine Enkephalin – A Mass Spectrometry Standard" (Sztáray et al., 2011). Leucine enkephalin is a simple pentapeptide having the tyrosine-glycine-glycine-phenylalanine-leucine (YGGFL) sequence that is biologically relevant (Hughes et al., 1975; Begley, 1996; Zlokovic, 2008). The protonated peptide fragments in a typical fashion, yielding many sequence ions: $[b_4]^+$, $[y_4 + 2H]^+$, $[a_4]^+$, $[b_3]^+$, $[y_2 + 2H]^+$, H^+Y , H^+F . and loss of H_2O . Among these, formation of $[b_4]^+$ is the lowest energy process. The decomposition of protonated YGGFL has been studied many times using many techniques, yet the article by Vekey and co-workers is notable because it manages to collect all these data, comparing and contrasting them, but ultimately drawing them together. The article shows that rate data taken over nine orders of magnitude can be interpreted self-consistently, despite individual studies providing Arrhenius activation energies (Ea) and pre-exponential factors (A) that differ appreciably. Their reanalysis of all these data, performed using their MassKinetics software (Drahos & Vékey, 2001), yielded activation parameters of Ea = 1.14 ± 0.05 eV (E₀ = 1.19eV) and $A = 10^{11.0 \pm 0.05}$ s⁻¹. This reanalysis also utilized a collision energy transfer distribution measured by Muntean and Armentrout (Muntean & Armentrout, 2001), adjusted from collisions with Xe to those with Ar, and shown to provide better agreement with experiments than alternative functions. Overall, the results provide one of the most definitive analyses of the decomposition of a protonated peptide available.

In the same spirit, my group has been interested in providing definitive thermodynamic and mechanistic information for the fragmentation of other cationized peptides. We believe this is achieved by a detailed examination of the absolute reaction cross sections (σ) for such reactions as a function of the energy (E) available using guided ion beam tandem mass spectrometry (GIBMS). Such σ (E) information can readily be converted to rate constants (k) at arbitrary temperatures (T) by multiplying by velocity (v), k (E) = v σ (E) and k (T) = <k (E)>MB, where the brackets indicate convolution over a Maxwell-Boltzmann (MB) distribution at the desired temperature. In this review, I compare and contrast GIBMS results for three types of systems: 1)

protonated and alkalated amino acids, 2) protonated and alkalated peptides containing mostly glycine (Gly, G) with extensions to alanine (Ala, A) and proline (Pro, P); and 3) dipeptides containing asparagine (Asn, N).

2 EXPERIMENTAL APPROACH

2.1 General

GIBMS has been used throughout the experimental work reviewed here with details of the instruments previously published (Ervin & Armentrout, 1985; Muntean & Armentrout, 2001). Specific conditions for each individual experiment are provided in the original publications. As an overview of the technique, the GIBMS instrument comprises an ion source, magnetic sector mass analyzer, ion-neutral interaction region, quadrupole mass filter (QMF), and ion detector. In nearly all cases considered here, the ion source is an electrospray ionization (ESI) source coupled to a radio frequency (rf) ion funnel (IF) and rf hexapole ion guide (6P) (Moision & Armentrout, 2007). In this source, ions generated by ESI are directed into vacuum through a capillary heated to 80 °C. The ions are collected by the IF (Kim et al., 2000) where they are collimated into a tightly focused beam and injected into the 6P. In this region, an in-source fragmentation method (Carl, Moision & Armentrout, 2009) can be used to generate fragment ions of the initial reagents. All ions in the 6P undergo ~10⁴ thermalizing collisions with the ambient gas at a pressure near 10⁻² Torr (residence time is tens of ms). As a consequence, the reactant ions are believed to have internal energies accurately described by a Maxwell-Boltzmann distribution at 300 K. This assumption has been demonstrated several times (Carl, Moision & Armentrout, 2007; Moision & Armentrout, 2007; Heaton & Armentrout, 2008b; Heaton & Armentrout, 2008a; Ye & Armentrout, 2008a; Carl, Chatterjee & Armentrout, 2010; Armentrout & Heaton, 2012a; Mookherjee, Van Stipdonk & Armentrout, 2017; Mookherjee & Armentrout, 2019).

Once the ions are formed, they are focused into the magnetic sector momentum analyzer. Because the ions are accelerated to a constant energy, this device provides mass selection of the desired reactant ion with good transmission and approximately unit mass resolution. Ions are then

decelerated using an exponential retarding stack of lenses and focused into a radio frequency (rf) octopole ion beam guide (Teloy & Gerlich, 1974; Gerlich, 1992). This device radially traps the ions without changing the axial kinetic energy of the ions in the laboratory frame. The latter is controlled by the voltage bias applied to the octopole, which can be varied over about four orders of magnitude. Part of the octopole is surrounded by a collision cell containing the reactant neutral at relatively low pressures, such that single collision conditions are approximated. This is verified by conducting experiments at several pressures of the neutral and extrapolating the cross sections obtained to zero pressure, rigorously single collision conditions. Because the octopole extends beyond the reaction cell in both directions, collisions between the ions and neutral reactants occur only at well-controlled kinetic energies, avoiding regions where ions are focused and accelerated.

After the collision cell, all ions drift to the end of the octopole where they are focused into the QMF to separate the ionic reactants and products. Ion transmission is optimized in the QMF so that all ions are collected as efficiently as possible. Ions are detected using a Daly-type detector (Daly, 1960) equipped with a high voltage (~25 kV) primary dynode. This ensures near unit detection efficiency for ions in our available mass range (up to ~300 Da). Intensities of all reactant and product ions are recorded as a function of the laboratory bias voltage applied to the octopole. The zero of this energy scale is ascertained in each experiment by scanning the applied voltage through the voltage of the ion source, such that ions with insufficient energy are no longer transmitted. Differentiation of this ion intensity curve can be modeled with a Gaussian peak, which provides the zero of energy in the reaction zone as well as the width of the kinetic energy distribution of the ions. For the ESI source, the absolute zero of energy can be determined within about 0.05 eV in the laboratory frame and the full width at half maximum (FWHM) of the distribution is generally 0.1 - 0.2 eV. The absolute kinetic energy of the ions in the laboratory frame, E_{lab} , is then converted to the center-of-mass frame energy, E_{CM} , by the equation $E_{CM} = E_{lab}$ \times m / (m + M). Here, m is the mass of the neutral reagent and M is the reactant ion mass. E_{CM} is the energy available to induce chemical reactions. In addition, the raw ion intensities are converted to absolute reaction cross sections (σ) after subtracting any background signal (resulting from noise and collisions outside the collision cell). This requires knowing the length of the interaction region (ℓ) and the density of the neutral gas (ρ) , which are both known to an accuracy of about 10%. This conversion utilizes an analogue of the Beer-Lambert law, $I = I_0 \exp(-\rho\sigma\ell)$, detailed as described previously (Ervin & Armentrout, 1985). Here, I equals the intensity of reactant ions after reaction and I_0 equals the intensity of reactant ions before reaction, treated as $I + \Sigma I_j$, where I_j is the ion intensity for a single product channel. Individual product cross sections (σ_j) are then provided by $\sigma_j = \sigma I_j / \Sigma I_j$.

2.2 Types of Reaction

A key concept in understanding (and therefore accurate modeling) of the decomposition processes considered here is whether the rate-limiting transition state (TS) for a particular channel is "tight" or "loose". A tight TS (TTS) is one that most chemists ordinarily think of, namely, a specific orientation of the molecule that has an imaginary frequency (the reaction coordinate) that leads either back to a precursor intermediate or on to a subsequent intermediate that moves towards products. In contrast, a loose TS does not have a well-defined imaginary frequency and, in the limit of no angular momentum, corresponds to the separated products. Such a loose TS is sometimes called an "orbiting TS" in the literature. As the angular momentum rises above zero (as it must in real reactions), there will be a centrifugal barrier along the potential energy surface that can be viewed as the effective TS. Such a loose TS has a high density of states because degrees of freedom that were vibrations in the precursor intermediate have become rotations in the TS. As a consequence, reactions that occur over loose TSs are entropically much more favorable than reactions that require a TTS. This contrast can easily be observed experimentally, as discussed further below.

2.3 Data Modeling

GIBMS allows ion-molecule reactions to be studied over a wide range of kinetic energies (about four order of magnitude) while maintaining good collection and detection efficiency. Thus,

the cross sections obtained can be confidently modeled to extract thermodynamic and mechanistic information. The modeling procedure is well described in previous work (Rodgers, Ervin & Armentrout, 1997; Rodgers & Armentrout, 1998; Armentrout, 2007), and details are generally provided in the individual studies as well. Eq. (1) is used to model cross sections for each product channel *j*.

$$\sigma_{j}(E) = \frac{n\sigma_{0}}{E} \sum_{i} g_{i} \int_{E_{0,j} - E_{i}}^{E} \frac{k_{j}(E^{*})}{k_{tot}(E^{*})} \left\{ 1 - e^{-k_{tot}(E^{*})\tau} \right\} (E - \varepsilon)^{n-1} d(\varepsilon)$$
 (1)

Here, σ_0 is an adjustable scaling parameter that is energy-independent, n is an adjustable parameter that characterizes the energy deposition efficiency during a collision (Muntean & Armentrout, 2001), E is the relative (CM) kinetic energy of the reactants, $E_{0,i}$ is the threshold energy for channel jat 0 K, and ε is the energy transferred from translational motion to internal energy of the reactant ion complex resulting from a collision with Xe. The summation in Equation (1) includes all populated rotational and vibrational states of the reactant ions, i, such that E_i is the energy of each state and g_i is the population of each ($\Sigma g_i = 1$). The total energy of the reactant ion after collision, the energized molecule (EM), is given by $E^* = \varepsilon + E_i$. The term enclosed within curly brackets in Eq. (1) refers to the probability of EM dissociation (P_{DI}) , where τ is the experimental time available $(\sim 5 \times 10^{-4} \text{ s according to time-of-flight studies})$ (Muntean & Armentrout, 2001). Thus, Equation (1) accounts for the lifetime of EM dissociation, which can delay the onset of the product ion formation. Such a "kinetic shift" generally increases as the reactant ion becomes larger. Equation (1) also directly models competition among parallel decomposition pathways because it incorporates the branching ratio term, $k_j(E^*)/k_{tot}(E^*)$. The rate constants (k) are determined by using Rice-Ramsperger-Kassel-Marcus (RRKM) theory, as shown in Equation (2) (Robinson & Holbrook, 1972; Gilbert & Smith, 1990).

$$k_{tot}(E) = \sum_{j} k_{j}(E^{*}) = \sum_{j} \frac{s_{j} N_{j}^{\dagger} (E^{*} - E_{0,j})}{h \rho(E^{*})}$$
 (2)

Here, s_j is the reaction degeneracy of channel j, N_j ^t is the sum of rotational and vibrational states of the TS for channel j with an energy $E^* - E_{0,j}$, ρ (E^*) refers to the density of states of the EM at

an available energy of E^* , and h is Planck's constant. Quantum chemical calculations are used to determine values for rotational constants and vibrational frequencies needed to evaluate N_j^{\dagger} ($E^* - E_{0,j}$) and ρ (E^*). These values are determined using the Beyer-Swinehart-Stein-Rabinovitch algorithm (Beyer & Swinehart, 1973; Stein & Rabinovitch, 1973; Stein & Rabinovich, 1977).

For reactions involving rate-limiting tight TSs (TTSs), molecular parameters are obtained directly from theoretical calculations. For reactions with rate-limiting loose TSs, frequencies of the TSs are assumed to equal those of the fully dissociated products with transitional frequencies treated as rotors, i.e., in the phase space limit (PSL) (Rodgers, Ervin & Armentrout, 1997; Rodgers & Armentrout, 1998). All external rotations are treated adiabatically while taking centrifugal effects into account (Waage & Rabinovitch, 1970). Generally, a statistical distribution summed across all possible values of the rotational quantum number is used to determine the appropriate rotational energy. Finally, for PSL TSs, the EM should have enough time to rearrange to the ground conformers of the products after collisional excitation, such that the measured $E_{0,j}$ is assumed to correspond to formation of the lowest energy conformer of the products.

In addition to primary product formation, some products undergo further (sequential) dissociation. Cross sections for such processes are not modeled as easily because the initial dissociation leads to uncharacterized internal and kinetic energy distributions of the primary products. Treating the primary product ion statistically allows an estimation of its internal energy such that the probability of the sequential dissociation (P_{D2}) can be treated similarly to that above (Armentrout, 2007). This statistical approach has proven to be adequate in a number of systems (with examples that include most of the molecules described below). Importantly, this analysis is designed for cases where the first dissociation occurs over a PSL TS. When the initial dissociation involves a TTS, energy can be released into internal and kinetic energy of the products in a manner than is uncharacterized. In such cases, the energies available to the sequential dissociation are no longer accurately described by the statistical assumptions.

Before comparison with the cross section data, the model of Equation (1) is convolved with the energy broadening associated with the thermal motion of the neutral collision partner (generally Xe) (Doppler broadening) and the kinetic energy distribution of the reactant ion (Ervin & Armentrout, 1985). Then, a nonlinear least-squares regression analysis is used to optimize σ_0 , n, and $E_{0,j}$. Uncertainties in these quantities (listed as one standard deviation throughout this manuscript) are determined by modeling multiple data sets, by varying the best fit n up and down by ~10%, scaling vibrational frequencies of the EM and TSs up and down by 10%, scaling τ up and down by a factor of 2, and by taking into account the absolute uncertainty in the energy scale. This procedure yields energy thresholds at 0 K for each decomposition pathway (Dalleska, Honma & Armentrout, 1993; Khan et al., 1993; Rodgers, Ervin & Armentrout, 1997; Rodgers & Armentrout, 1998; Armentrout, 2002; Armentrout, 2007; Carpenter et al., 2017).

2.4 Computational Details

As noted above, the analysis of the data requires vibrational frequencies and rotational constants of the reactant ions and the product TSs. Although these could be guessed with reasonable accuracy, the advent of quantum chemistry programs allows better estimates of these quantities. (Despite this, we find that it is sometimes necessary to adjust frequencies of TTSs in order to accurately reproduce the data. Generally, this is accomplished by adjusting low frequencies, those below ~900 cm⁻¹, which are not as accurately predicted as vibrations at higher frequencies.) Further, these calculations can then provide more detailed mechanistic information for comparison to the experimental results, as well as yielding independent estimates of the thermochemistry. Comparison of the theoretical thermodynamics to that extracted from analysis of the GIBMS experiments can then verify that the appropriate mechanism has been identified as well as ascertaining the structure of many of the products observed.

Although the computational approaches used in our group have evolved over the years, they have generally involved the following protocol. Possible structures of reactants and products are explored using a simulated annealing program, most recently using the Amber 14 force field. Relaxed potential energy surface scans are then often performed to search for alternative conformers and isomers of reactants, TSs, intermediates, and products. Generally, these structures

are then geometry optimized to obtain vibrational frequencies (used to provide zero point energy and thermal corrections to all single point results) and rotational constants at the B3LYP/6-311+G(d,p) level of theory (Hehre, 1976; Lee, Yang & Parr, 1988; Becke, 1993) with a Berny optimization (Schlegel, 1982). Single-point energies are calculated at the B3LYP, B3P86, and MP2(full) (where full refers to the correlation of all electrons, abbreviated as MP2 below) levels of theory with the 6-311+G(2d,2p) basis set and sometimes at additional levels as well. These levels of theory and basis sets have been shown to provide accurate comparison with experimental energies in many of the systems discussed below (Armentrout, Heaton & Ye, 2011; Armentrout & Clark, 2012; Armentrout & Heaton, 2012a; Armentrout & Heaton, 2012b; Mookherjee, Van Stipdonk & Armentrout, 2017; Mookherjee & Armentrout, 2019).

3 ALKALI METAL CATIONIZED AMINO ACIDS AND GLYCINE BIOPOLYMERS

Our group and others have studied a number of amino acids (AAs) cationized with alkali ions (M⁺). Measurements of binding energies have been performed using the kinetic method (Bojesen, Breindahl & Andersen, 1993; Kish, Ohanessian & Wesdemiotis, 2003; Wang, Ohanessian & Wesdemiotis, 2008; Tsang et al., 2012; Bourcier et al., 2015), thermal equilibrium (Gapeev & Dunbar, 2001; Gapeev & Dunbar, 2003), and TCID (Klassen et al., 1996; Moision & Armentrout, 2002; Ruan & Rodgers, 2004; Moision & Armentrout, 2006; Heaton & Armentrout, 2008b; Heaton & Armentrout, 2008a; Heaton, Moision & Armentrout, 2008; Ye & Armentrout, 2008b; Ye, Clark & Armentrout, 2008; Armentrout, Gabriel & Moision, 2009; Armentrout et al., 2010a; Armentrout et al., 2010b; Bowman, Heaton & Armentrout, 2010; Armentrout, Chen & Rodgers, 2012; Armentrout et al., 2012; Armentrout, Yang & Rodgers, 2013; Shoeib et al., 2013; Armentrout, Yang & Rodgers, 2014; Mookherjee & Armentrout, 2014; Clark et al., 2019). Most of these thermodynamic data have been compiled recently (Rodgers & Armentrout, 2016a). In addition, many of these systems have had their structures interrogated using infrared multiple photon dissociation (IRMPD) action spectroscopy (Kapota et al., 2004; Polfer et al., 2005; Polfer, Oomens & Dunbar, 2006; Bush et al., 2007a; Bush et al., 2007b; Forbes et al., 2007; Armentrout

et al., 2008; Bush et al., 2008; Drayss et al., 2008; O'Brien et al., 2008; Rodgers et al., 2008; Bush, Oomens & Williams, 2009; Heaton et al., 2009; Carl et al., 2010; Citir et al., 2010; Drayss et al., 2010; Dunbar, Steill & Oomens, 2010; Citir et al., 2012).

3.1 Lithiated amino acids

In most of the M⁺AA systems, dissociation of these complexes occurs by loss of the intact amino acid yielding the metal cation. The threshold measured for dissociation equals $D_0(M^+-AA)$. In contrast, lithiated amino acids will often dissociate via pathways similar to the protonated species because of the high binding energy of the small lithium cation. Siu and co-workers found that Li⁺Phe, Li⁺Tyr, Li⁺Trp, and Li⁺His all exhibited a number of fragmentations (losses of H₂O, H₂O + CO, NH₃ + CO, NH₃ + CO₂, LiOH, and side-chains) but did not characterize the kinetic energy dependence of these reactions, although they did examine this for the analogous Ag⁺ complexes (Shoeib et al., 2013). Li⁺Ser and Li⁺Thr exhibit losses of H₂O, CO₂, H₂O + CO, H₂O + CO_2 , and RCHO where R = H and CH_3 , respectively (Ye & Armentrout, 2008b). Thresholds for losses of H₂O, CO₂, and RCHO were measured and lie about 1 eV below the binding energy of the intact AA. Comparison with theory allowed the identification of most of the fragments formed. For Li⁺Cys (Armentrout et al., 2010b), in addition to loss of Cys, the complex also deaminates yielding both Li⁺(C₃H₄O₂S) and Li⁺(NH₃). Measurement of the threshold energies for all three processes determines binding energies to all three ligands and comparison with theory identifies the C₃H₄O₂S species as the thiirane-carboxylic acid. For both Li⁺Pro and Li⁺(N-methyl-Pro) (Moision & Armentrout, 2006; Mookherjee & Armentrout, 2013; Mookherjee & Armentrout, 2014), the systems lose CO (an intermediate not observed) followed by either H₂O or LiOH, in competition with a higher energy loss of the intact AA, Figure 1. Experiment and theory show that the loss of CO + H₂O is favored energetically but requires more rearrangement, such that loss of CO + LiOH is entropically favored. These pathways for dissociation yield lithiated and protonated C₄H₇N and C₅H₉N fragments. These fragments were identified as pyrrolines on the basis of computational mechanisms that yielded results in agreement with the experimentally measured

thermochemistry. Finally, decomposition of Li⁺Lys has been examined using GIBMS (Clark et al., 2019). Here, nine channels were observed to compete with loss of neutral Lys, with loss of NH₃ being the dominant pathway. Previous labeling work of protonated Lys has shown that this ammonia originates from the side-chain amine (Milne, Axenrod & Fales, 1970) and leads to cationized 2-amino-5-hexenoic acid, a derivative of norleucine.

3.2 Sodiated and potassiated amino acids

In their study of cationized aromatic amino acids, Shoeib et al. (Shoeib et al., 2013) found that Na⁺Phe and Na⁺Tyr dissociated exclusively by loss of the intact amino acid, whereas Na⁺Trp and Na⁺His exhibited small amounts of other fragments (losses of NH₃, NH₃ + CO, the side chain). For the acidic amino acids (aspartic acid, Asp, and glutamic acid, Glu) and their amide derivatives (asparagine, Asn, and glutamine, Gln), decomposition of the sodiated complexes again shows predominantly loss of the intact AA, but Na⁺Glu shows a prominent loss of water at low energies, Na⁺Asn also loses ammonia at slightly lower energies than Asn loss, and Na⁺Gln shows prominent losses of H₂O and NH₃ with comparable efficiencies (Heaton, Moision & Armentrout, 2008). In a related study, these decompositions (as well as dehydration of Na⁺Asp) were induced in the source and the product species were then probed experimentally (Heaton, Ye & Armentrout, 2008). Comparison of the experimental binding energies of the dehydration and deamidation products with computed thermochemistry demonstrated that Asp and Asn dissociated to form the aminosuccinic anhydride (aSA), and Gly and Gln formed oxo-proline (O-Pro). These species and the measured binding energies to Na⁺ are shown in Figure 2 along with the Na⁺ binding energies to water, ammonia, and the four amino acids. Alternative structures for the dehydration and deamidation products yield theoretical Na⁺ binding energies that do not agree with experiment.

A more extensive study of the Na⁺Asn complex (Heaton & Armentrout, 2008b; Heaton, Moision & Armentrout, 2008) explored the deamidation process more completely. The results are shown in Figure 3 along with the modeling. The threshold for forming Na⁺ + Asn yields the sodium binding affinity shown in Figure 2. The threshold for deamidation forming Na⁺aSA + NH₃, 155 \pm

8 kJ/mol, corresponds to the TTS shown in Figure 4, whose energy could be reproduced at several levels of theory. In this TTS, the ammonia leaving group is displaced by an S_N2-like attack of the carbonyl oxygen forming the five-membered ring in aSA. Finally, the decline in the Na⁺aSA cross section could only be modeled assuming decomposition to Na⁺ + aSA, which yields a lower limit to the Na⁺-aSA binding energy, again in good agreement with this structural assignment and the calculated potential energy surface for deamidation. This observation sparked our interest in this important deamidation process, leading to the studies outlined in Section 6.

In our studies to date, no complexes of amino acids with Rb⁺ and Cs⁺ have been observed to dissociate by any path except loss of AA, clearly because of the weaker binding of these alkali cations. The same holds true for K⁺, with a single exception. In analogy with the results for Na⁺Gln, K⁺Gln dissociates by losses of both H₂O and NH₃; however, these pathways are less prominent than in the sodiated case (Heaton & Armentrout, 2008a). Although not explored computationally, it seems clear that these dissociations lead to analogous products as in the sodiated case. Overall, periodic trends in these alkali cation affinities have been discussed extensively in the literature (Rodgers & Armentrout, 2016a; Rodgers & Armentrout, 2016b).

3.3 Sodiated and potassiated diglycine and triglycine

For small peptides, only sodiated and potassiated GG and GGG have been examined by TCID methods (Ye & Armentrout, 2008a). Previous work on such systems included measurements of the Na $^+$ GG binding energy by CID (Klassen et al., 1996) and kinetic method (Cerda et al., 1998; Feng, Gronert & Lebrilla, 1999; Kish, Wesdemiotis & Ohanessian, 2004) yielding 298 K values of 180 ± 10 , 177 ± 10 , 186, and 203 ± 8 kJ/mol, respectively. Our study measured 211 ± 13 kJ/mol, in agreement with the most recent of these values. Likewise, our 298 K value for the Na $^+$ GGG binding energy of 241 ± 17 kJ/mol matches that determined by the kinetic method study of Wang et al. (Wang et al., 2007), 237 ± 9 kJ/mol. The GIBMS study also determined potassium cation binding energies to GG and GGG as 150 ± 7 and 183 ± 16 kJ/mol, respectively, along with a GNa $^+$ -G bond energy of 124 ± 10 kJ/mol (Ye & Armentrout, 2008a).

Among these systems, the only complex that dissociates by a route other than loss of the intact ligand is Na $^+$ GGG. In addition to forming Na $^+$, this species also yields the Na $^+$ G product ion as shown in Figure 5. Although a detailed analysis of this channel was not performed in this work, it is clear that the Na $^+$ G product has a slightly lower threshold than the formation of Na $^+$ at 2.49 \pm 0.18 eV (240 \pm 17 kJ/mol). The relative magnitude of the Na $^+$ G cross section suggests it is entropically disfavored compared to the PSL TS associated with Na $^+$ + GGG formation. In analogy with protonated GGG (see Section 5.2), Na $^+$ G is the equivalent of the [y₁+2H] $^+$ product, which suggests that the neutral formed is 2-aminomethyl-5-oxazolone, AMOx, Figure 4. Further, the failure to observe Na $^+$ AMOx, the [b₂] $^+$ product analogue, suggests that sodium binds to glycine more tightly than to AMOx. This can be justified because Na $^+$ binds to glycine by bridging the carbonyl oxygen and amine nitrogen (Moision & Armentrout, 2002; Kapota et al., 2004). The only likely bridging position in AMOx is between the two nitrogens, which should bind less strongly. Indeed, calculations at the MP2(B3LYP)/6-311+G(2d,2p)//B3LYP/6-311+G(d,p) level performed here indicate that sodium cations bind AMOx more weakly than glycine by 3.5 (6.6) kJ/mol.

4 PROTONATED AMINO ACIDS

In these studies, we have performed TCID studies on protonated glycine, H⁺Gly (Armentrout, Heaton & Ye, 2011), protonated cysteine, H⁺Cys (Armentrout & Stennett, 2014), and protonated asparagine, H⁺Asn (Heaton & Armentrout, 2009), determining both the energetics and mechanisms for decomposition. The kinetic energy dependence of protonated amino acid fragmentation has been examined for many more amino acids by Dookeran, Yalcin, and Harrison (Dookeran, Yalcin & Harrison, 1996), who formed their ions using fast atom bombardment and discussed possible mechanisms; Rogalewicz, Hoppilliard, and Ohanessian (Rogalewicz, Hoppilliard & Ohanessian, 2000) and El Aribi, Orlova, Hopkinson, and Siu (Aribi et al., 2004), who both used ESI to form their ions and included theoretical explorations of the possible mechanisms; and Zhang et al. (Zhang et al., 2019), who used ESI and high-resolution MS in order to identify new pathways and remove ambiguities in some fragmentation assignments. Unlike the

GIBMS work, none of these studies determined the energetics of the fragmentation processes. Notably, the observed agreement between the experimental and theoretical energies for these decompositions (and those in Sections 5 and 6 as well) supports that the key steps involved in their mechanisms have been properly identified and, further, is direct support of the mobile proton model that allows an understanding of peptide dissociation chemistry (Burlet et al., 1992; Cox, 1996; Dongré et al., 1996; Wysocki et al., 2000).

4.1 Protonated Glycine

Protonated glycine (H⁺G) is a useful starting point for the examination of protonated peptides because of its simplicity. Like all protein and peptides, it has an amino group N-terminus and a carboxylic acid C-terminus. Thus, all protonated peptides will generally include the dissociation processes observed here, although the mechanism does change. TCID results for H⁺G are shown in Figure 6 (Armentrout, Heaton & Ye, 2011) and exhibits two products, loss of CO to form 48 *m/z*, and loss of CO + H₂O to form 30 *m/z*. The TCID results clearly indicate that these are sequential processes, with the loss of CO occurring at lower energies, followed by the additional loss of water as the energy is increased. These results are qualitatively similar to those of Klassen and Kebarle (Klassen & Kebarle, 1997), who used a triple quad mass spectrometer. The GIBMS results have superior signal to noise that allows an accurate differentiation of the lowest energy channel. These results are also consistent with those of Wesdemiotis and co-workers (Beranova, Cai & Wesdemiotis, 1995), who observed a major peak at 48 *m/z* in their metastable ion spectrum, giving way to 30 *m/z* in their higher-energy collisionally-activated dissociation (CAD) spectrum.

The mechanism for dissociation of H⁺G has been theoretically examined a number of times (Uggerud, 1997; O'Hair et al., 2000; Armentrout, Heaton & Ye, 2011), with consistent results. In its lowest energy structure, the ground structure (GS), H⁺G is protonated on the amino group, Figure 6. In the rate-limiting TS, this proton transfers to the hydroxy group to form water, which also weakens the C-C bond. In a second TS lying slightly below the first one, the C-C bond cleaves

generating $CH_2=NH_2^+$, the $[a_1]^+$ product ion, bound to H_2O and CO. The CO binds more weakly to $CH_2NH_2^+$ than water and therefore is lost more readily; indeed, the putative $CH_2NH_2^+(CO)$ complex was not observed in our work despite careful attempts to locate this product. According to theory, the final $[a_1]^+ + CO + H_2O$ products are nearly equal in energy to the rate-limiting TS, whereas the 48 m/z product lies well below this TS. Thus, the threshold observed for the latter product is a measure of the TS energy, calculated to be 132 (MP2) and 144 (B3LYP) kJ/mol. The modeling of the data is shown in Figure 6, where it can be seen that the branching between the two channels is accurately reproduced over a wide range of energies and cross section magnitudes. (Similar reproductions of the data in the following sections are also obtained by our approach, but will not be included in the following diagrams as they make the figures too complex.) The threshold obtained from this analysis is $160 \pm 5 \text{ kJ/mol}$, somewhat higher than the theoretical values but otherwise in reasonable agreement.

This analysis also yields a threshold for formation of the $[a_1]^+$ product ion, but Wesdemiotis and co-workers showed that release of CO occurs non-statistically with an average kinetic energy release of 44 kJ/mol (Beranova, Cai & Wesdemiotis, 1995). (Another example of this phenomenon is decomposition of the $[b_2]^+$ ion formed from protonated GlyProAla, discussed in Section 5.5.) Thus, the statistical analysis shown in Figure 6 should not yield accurate thermochemistry for the 30 m/z channel. Rather, we analyzed the branching ratio of the two products above the initial threshold energy as the statistical decomposition over loose PSL TSs of the $CH_2NH_2^+(H_2O)(CO)$ complex. This model also reproduces the data well and yields a threshold for $[a_1]^+$ of 140 ± 8 kJ/mol. This value compares well with a literature experimental value of 139.0 ± 8.2 kJ/mol, determined from the relative proton affinities of glycine and CH_2NH , as well as with theory: 137 kJ/mol (MP2 and B3LYP) (Armentrout, Heaton & Ye, 2011).

4.2 Protonated cysteine

Once the side chain of the amino acid acquires a heteroatom, additional decomposition channels become available. In the case of protonated cysteine, H⁺Cys, TCID results are shown in

Figure 7 (Armentrout & Stennett, 2014). These results demonstrate that the loss of $H_2O + CO$ is still active, but now competes with deamination, a channel where either the $C_3H_4O_2S$ or NH_3 product can retain the proton, with the latter being favored. Subsequent channels include losses of $NH_3 + H_2O$, $NH_3 + H_2O + CO$, $H_2O + CO + HS$, and other minor products at the highest energies examined (26, 28, and 35 m/z). These results are in general agreement with previous studies (Dookeran, Yalcin & Harrison, 1996; O'Hair, Styles & Reid, 1998; Rogalewicz, Hoppilliard & Ohanessian, 2000) although the studies of Dookeran et al. and Rogalewicz et al. did not observe the NH_4 ⁺ product and this channel is relatively small in the work of O'Hair et al. Zhang et al. (Zhang et al., 2019) also found 88 m/z, but this product is much less abundant than the 87 m/z product and would not have been observed easily in our work.

Extensive theoretical work on the mechanisms for H⁺Cys decomposition was conducted by O'Hair et al. and by our group, with similar qualitative findings. For loss of H₂O + CO, a proton is transferred from the protonated amine group to the hydroxy group via one of six pathways. The TTS for this transfer is calculated to lie well above the energy for loss of both H₂O and CO, hence the individual losses are not observed, and the threshold measured for this channel corresponds to the TTS energy. The product formed is HSCH₂CH=NH₂⁺, the 1-amino-2-mercapto-ethylium cation. Deamination is also limited by a TTS, which is reached by protonating the amine group and then displacing ammonia by an S_N2-type attack of sulfur at the alpha carbon, which forms a three-membered cyclic thiirane with a carboxylic acid substituent complexed to ammonia. To form the final products, we find that the ammonia must transfer so that it interacts with the HS group, which requires another 10 – 16 kJ/mol. This forms several forms of the thiirane-carboxylic acid (TICA) bound to NH₄⁺. Dissociation to NH₄⁺ + TICA requires less energy than the rate-limiting step, hence the threshold for formation of NH₄⁺ corresponds to this TTS. At slightly higher energies, the proton can be retained by TICA on the sulfur, yielding the 105 m/z channel. Mechanisms for the subsequent dissociations to form 87, 59, and 43 m/z (not explored previously) were also elucidated in our work. Agreement between the experimental thresholds measured and those calculated at the MP2 level for the six major products (mean absolute deviation of 8 ± 4 kJ/mol) verified that the pathways and structures of the products located theoretically were reasonable.

4.3 Protonated asparagine

As for H⁺Cys, protonated asparagine, H⁺Asn, undergoes the primary pathways of losing H_2O (115 m/z), $H_2O + CO$ (87 m/z), and ammonia yielding both NH₄⁺ (18 m/z) and 116 m/z, Figure 8 (Heaton & Armentrout, 2009). At higher energies, the 116 m/z product dissociates further, mainly by loss of ketene to yield 74 m/z, but also by loss of CO to form 88 m/z. Minor products at 60 and 44 m/z were also quantified. Although this system had been studied previously by both Dookeran et al. and Rogalewicz et al. (Dookeran, Yalcin & Harrison, 1996; Rogalewicz, Hoppilliard & Ohanessian, 2000), neither study observed the major NH₄⁺ product or the minor products at 60 and 44 m/z, and each missed one of the other products as well (88 and 115 m/z, respectively). Here, because there are two NH₂ groups in Asn, the ammonia loss could conceivably be deamination (N-terminus loss) or deamidation (side chain loss). The mechanism for H₂O and CO loss had not been explored for H⁺Asn in detail before, although it parallels work done on other protonated AAs. As for both H⁺Gly and H⁺Cys, the rate-limiting TTS involves proton transfer from the protonated N-terminus to the hydroxy group but now the carbonyl side chain assists the loss of water by forming a five-membered furanone ring, 3-amino-5-imino-2-furanone protonated at the imine nitrogen, Figure 4. The formation of the 115 m/z product ion is limited by this TTS. Slightly more energy then leads to the loss of CO and generation of H₂NC(=O)CH₂CH=NH₂⁺, the [a₁]⁺ product. Theory indicates that loss of ammonia is a deamidation process, which occurs by reorienting the molecule so that the carboxylic acid can donate its proton to the amide nitrogen, thereby forming the ammonia leaving group. The rate-limiting TTS (TS_N) then involves concerted ammonia loss and formation of the succinic anhydride ring, Figure 4, yielding a proton bound dimer of amino-succinic anhydride (aSA) and ammonia. Protonated aSA is stabilized by protonating the carbonyl oxygen than can hydrogen bond to the amino group. Thus, aSA has a higher proton affinity than ammonia, such that the NH₄⁺ + aSA products lie slightly below the rate-limiting TTS with NH₃ + H⁺aSA products lying slightly above this TTS. In this study, the competitive channels of 116, 115, 87, and 18 *m/z* were all successfully modeled and yielded threshold energies in good agreement with the theoretical pathways (within 10 kJ/mol), thereby verifying the mechanisms and product structures located.

One interesting aspect of the TTS for deamidation of H⁺Asn is that the proton is located remotely from the location of the ring closure. Further, this study was inspired by our observation that Na⁺Asn also deamidates, as described above in Section 3.3. The TTSs for these two deamidations are compared in Figure 4 and can be seen to be directly parallel. This comparison suggests that the charge carrier and its location are *not* the key elements of the deamidation process in these small molecules, such that the mechanism elucidated here is plausibly useful for understanding deamidation of larger systems. Hence, we initiated studies of the deamidation of the protonated AsnXxx dipeptides, described in Section 6.

5 PROTONATED GLYCINE BIOPOLYMERS AND RELATED SPECIES

We have performed TCID studies on protonated diglycine, H⁺GG (Armentrout & Heaton, 2012a; Armentrout & Heaton, 2012b), protonated triglycine, H⁺GGG (Mookherjee, Van Stipdonk & Armentrout, 2017), protonated GlyAlaGly (H⁺GAG) (Mookherjee & Armentrout, 2019), protonated GlyGlyAla (H⁺GGA), and protonated GlyProAla, H⁺GPA (Jones, Boles & Armentrout, 2020). Here, we examine how the length of the peptide influences the fragmentation observed and how simple substitutions (Ala or Pro for Gly) can change the energetics significantly.

5.1 Protonated Diglycine

Unsurprisingly, the TCID spectrum of protonated diglycine, H⁺GG, is more complicated than that for H⁺G, Figure 9 (Armentrout & Heaton, 2012b). There are two primary dissociation channels: loss of water to form 115 m/z, the $[b_2]^+$ ion, and loss of CO to form 105 m/z, which can be shown to be a proton bound dimer of CH₂NH and G. At higher energies, the $[b_2]^+$ product loses CO to form $[a_2]^+$ at 87 m/z. Given the structure of the 105 m/z product, dissociation to form H⁺G

 $([y_1+2H]^+, 76 \, m/z) + \text{CH}_2\text{NH}$ and CH_2NH_2^+ $([a_1]^+, 30 \, m/z) + \text{G}$ is efficient. Clearly, G has a higher proton affinity (PA) than CH₂NH, which is why the former product dominates at low energy. This observation is consistent with experimental measurements and theoretical calculations of these PAs, which places PA(G) about 23 kJ/mol higher than PA(CH₂NH), see discussion in (Armentrout, Heaton & Ye, 2011). This rapid dissociation also explains why the 105 m/z product cross section never gets very large. In addition to forming $[a_1]^+$ from 105 m/z in competition with H⁺G, it can also be realized that H⁺G dissociates to form $[a_1]^+$ (see Figure 6), and modeling of the H⁺GG data confirms this. The decarbonylation product 105 m/z also dissociates by loss of ammonia to yield 88 m/z, but this process is much less efficient that those leading to 76 and 30 m/z, suggesting it is entropically disfavored.

The mechanism for H⁺GG dissociation has been examined several times (Klassen & Kebarle, 1997; Paizs et al., 2001; Paizs & Suhai, 2001b; Balta, Aviyente & Lifshitz, 2003; Pingitore et al., 2004; Armentrout & Heaton, 2012a), with generally good agreement among the results. Like H⁺G, the initial decarbonylation reaction is initiated by transferring the proton originally on the N-terminus (Figure 9) to the central nitrogen, which forms glycine attached to CO attached to CH₂NH₂. Over the rate-determining TTS, the OC-CH₂NH₂ and OC-NH₂CH₂CO₂H bonds are broken simultaneously, leading to the proton bound dimer, CH₂NH₂⁺(G), with CO weakly attached. The TTS lies well above the energy needed to lose CO, whereas separation into the final $[y_1+2H]^+$ or $[a_1]^+$ products over loose PSL TSs requires considerably more energy. Modeling of the data confirms this with a threshold for formation of 105 m/z of 156 \pm 5 kJ/mol, in agreement with theory: 154 (B3LYP) and 168 (MP2) kJ/mol. Likewise modeling yields thresholds for the $[y_1+2H]^+$ or $[a_1]^+$ products that agree well with MP2 theory (Table 1). The competitive loss of NH₃ is found theoretically to require formation of a covalent C-N bond between CH₂NH₂⁺ and glycine followed by proton transfer to the terminal amino group, yielding the CH₂=NHCH₂CO₂H⁺ product at 88 m/z. The pathway is analogous to one located for H⁺AGG by Bythell et al. (Bythell et al., 2007).

The other primary reaction, initial loss of water, is found theoretically to involve proton transfer to the hydroxy group either from the N-terminus or from the protonated central carbonyl, both with similar TS energies. These TTSs are rate-limiting, which explains why this channel is smaller than those involving the PSL TSs evolving after decarbonylation. Unlike the H⁺G system, loss of water from H⁺GG is facilitated by an S_N2-like process in which the central carbonyl oxygen forms a bond with the terminal C, forming the five-membered oxazolone structure, H⁺AMOx, 115 m/z, Figure 4, protonated on the ring nitrogen such that a hydrogen bond with the amine is formed. (For the same reason, such backside attacks forming cyclic structures are prominent in the longer peptides as well.) This lowers the energy of the final products considerably. (The alternative structure of protonated diketopiperazine (H⁺DKP) was also considered but its calculated ratelimiting TTS lies another 89 - 97 kJ/mol above those for H⁺AMOx, which disagrees with the experimental threshold measured.) The TTSs for water loss lie well above the H⁺AMOx + H₂O product asymptote, such that further decomposition of H⁺AMOx occurs in the absence of the water product. Decarbonylation of H⁺AMOx leads to [a₂]⁺, CH₂=NHC(=O)CH₂NH₂⁺, which can rearrange to a cyclic form at higher energies, as demonstrated by IRMPD studies (Bythell, Maitre & Paizs, 2010; Verkerk et al., 2010).

5.2 Protonated Triglycine

Protonated triglycine, H⁺GGG, is among the most extensively studied small peptides. In addition to our own TCID study (Mookherjee, Van Stipdonk & Armentrout, 2017), Klassen and Kebarle (Klassen & Kebarle, 1997) and Aribi et al. (El Aribi et al., 2003) examined the kinetic energy dependence of its decomposition and Reid, Simpson, and O'Hair (Reid, Simpson & O'Hair, 1999) also performed MS/MS experiments. Theory was performed in all these studies, but was augmented by theoretical work of Rodriquez et al. (Rodriquez et al., 2001) and Paizs and Suhai (Paizs & Suhai, 2001a; Paizs & Suhai, 2002). In our TCID work, we characterized 10 different reaction channels both experimentally and theoretically, substantially extending the previous work.

The TCID cross sections for H⁺GGG are shown in Figure 10a. As for the smaller systems, loss of water to form the $[b_3]^+$ product ion at 172 m/z is observed followed at higher energies by loss of CO to yield $[a_3]^+$ at 144 m/z. The mechanism parallels that for H⁺GG and yields the protonated oxazolone, 2-glycylaminomethyl-5-oxazolone, H⁺GAMOx, as verified by good agreement between theory and experiment for the TTS leading to this species. Notably, this process has the lowest threshold energy, which is not at all evident from a cursory inspection of the data, Figure 10a. This is because the TTS suppresses the magnitude of this product cross section and leads to a strong kinetic shift, which moves the apparent threshold above that for formation of the $[b_2]^+$ ion, which is entropically favored because its formation occurs over a loose PSL TS. According to our theoretical explorations, the $[a_3]^+$ product formed by decarbonylation of $[b_3]^+$ is the linear amidated GGNH⁺=CH₂; however, a cyclic seven-membered ring form has been identified by IRMPD spectroscopy for the $[a_3]^+$ product from H⁺GGGG (Bythell, Maitre & Paizs, 2010). This study calculates that a barrier of 44 kJ/mol is required to convert from the linear form to the more stable (by 23 kJ/mol) cyclic form.

Also in direct parallel to the H⁺GG case described above, another major primary channel is decarbonylation. In this case, the H⁺GGG – CO product at 162 *m/z* is not observed experimentally (although it was explicitly looked for) because the subsequent products can be formed with very little additional energy. Once CO is lost, the product is a proton bound dimer of CH₂NH and GG, which readily dissociates via PSL TSs to H⁺GG, [y₂+2H]⁺ at 133 *m/z*, and to CH₂NH₂⁺, [a₁]⁺ at 30 *m/z*. Clearly, GG has a higher PA than CH₂NH. The coupling reaction leading to subsequent loss of NH₃ is also observed again, yielding the product at 145 *m/z*. As for H⁺GG, this reaction requires a TTS such that the magnitude of its cross section is suppressed by competition with the other two channels.

Identification of the $[y_2+2H]^+$ product as H⁺GG is confirmed by analysis of the thresholds compared with theory but also by the subsequent dissociations observed. As shown in Figure 9, H⁺GG dissociates to yield $[y_1+2H]^+$, $[a_1]^+$, and loss of CO (105 m/z). As in Figure 9, Figure 10a shows a small cross section for 105 m/z and a much larger cross section for $[y_1+2H]^+$. The second

feature in this $[y_1+2H]^+$ cross section can be identified as the sequential product (as denoted by the solid symbols). Although $[y_2+2H]^+$ also dissociates to form $[a_1]^+$, no obvious feature for this secondary pathway is observed because its cross section is dominated by the initial path noted above.

In addition to the channels that parallel those of H⁺GG, the H⁺GGG ion also dissociates by cleaving the first peptide bond leading to competitive formation of $[b_2]^+$ at $115 \, m/z$ and $[y_1+2H]^+$ at $76 \, m/z$ (the lower energy feature in Figure 10a). Here the mechanism involves proton migration to the amide nitrogen of the third residue, which forms an intact glycine molecule. Cleavage of this C-N bond is aided by nucleophilic attack of the first carbonyl oxygen at the second carbonyl carbon, thereby forming protonated AMOx and G. The proton bound dimer of these two species can then readily dissociate to either the $[b_2]^+$, H⁺AMOx, or $[y_1+2H]^+$, H⁺G, products over PSL TSs that lie well above the TTS leading to the proton dimer. Because the rate-limiting TSs for both products are loose (corresponding to the products), this explains the large magnitude of the $[b_2]^+$ product cross section. (The PSL TS for $[b_2]^+$ formation here contrasts with that for forming $[b_2]^+$ from H⁺GG because the latter is the water loss channel, which retains a TTS for H⁺GGG in formation of the $[b_3]^+$ product.) The $[y_1+2H]^+$ cross section is smaller because it lies at higher energy, thereby competing with the main $[b_2]^+$ product ion. Modeling of the data confirms this.

For this particular system, the identification of the $[b_2]^+$ product at H⁺AMOx was verified independently in another TCID study (Armentrout & Clark, 2012). Here, H⁺GGG was dissociated in the source region and its $[b_2]^+$ product ion was mass selected and subjected to CID with Xe. The $[b_2]^+$ product was found to dissociate primarily by CO loss yielding the $[a_2]^+$ product ion at 87 m/z. At still higher energies, the dominant product was $[a_1]^+$ although a small amount of its precursor, $[a_2]^+$ - CO at 59 m/z, the proton bound dimer of CH₂NH, was also observed. The relative magnitudes of these product cross sections are consistent with those observed in Figure 10a once the other pathways for $[a_1]^+$ are also considered. The kinetic energy resolved product spectrum was also compared to that for a sample of H⁺DKP and found to differ appreciably. H⁺DKP dissociates at much higher energies, yielding less $[a_2]^+$ as well as additional products not found for H⁺AMOx.

5.3 Protonated GlyAlaGly

The TCID spectrum for protonated GlyAlaGly, H⁺GAG, is shown in Figure 10b (Mookherjee & Armentrout, 2019). Mechanisms for dissociation parallel those found for H⁺GGG in all cases, and it can be seen that the major products observed are comparable to those for H⁺GGG. Nevertheless, the simple addition of a methyl group clearly influences the relative magnitudes of many product channels. The $[b_2]^+$ ion is more prominent, consistent with a threshold measured to be lower by 11 kJ/mol, as also found by theory, Table 1. This is because the $[b_2]^+$ is now a ring-methylated version of H⁺AMOx, H⁺MAMOx, which increases its PA and lowers its energy. (Notably, if $[b_2]^+$ formation were limited by a TTS, then the enhanced PA would be unlikely to shift the threshold as much.) The enhanced stability of the $[b_2]^+$ product clearly affects its competition with $[y_1+2H]^+$, which now has a much smaller cross section. The identity of the [b₂]⁺ product as H⁺MAMOx was confirmed by examining its dissociation independently, as outlined above for H⁺AMOx (Armentrout & Clark, 2012). This study shows that H⁺MAMOx dissociates first to $[a_2]^+$ at 101 m/z, and then at higher energies, to both $[a_1]^+$ and CH₃CH=NH₂⁺ at 44 m/z, with the latter dominating. These dissociations explain the enhanced $[a_2]^+$ cross section seen in Figure 10a as well as the $CH_3CHNH_2^+$ product and contributes to the $\lceil a_1 \rceil^+$ cross section. The fact that the $[a_1]^+$ (CH₂NH₂⁺) cross section is larger than that for CH₃CHNH₂⁺ indicates that the formation of $[a_1]^+$ from the primary reaction channel involving initial decarbonylation followed by competitive formation of $[a_1]^+$ and $[y_2+2H]^+$ is still important for H⁺GAG. It can be seen that the [y₂+2H]⁺ product channel is also smaller than in the H⁺GGG case, which is attributed to competition with the enhanced [b₂]⁺ primary channel. The same competition probably affects the magnitudes of the [b₃]⁺ and subsequent [a₃]⁺ ions, which are smaller for H⁺GAG. Modeling shows this is partly because the threshold energy for [b₃]⁺ formation increases slightly (by 11 kJ/mol). All changes measured in threshold energies for analogous processes between H⁺GGG and H⁺GAG are matched by theory except for the loss of CO where the signs differ although the absolute values are still within uncertainties: -7 ± 12 kJ/mol experimentally, but +6 to +11 kJ/mol from theory.

5.4 Protonated GlyGlyAla

TCID results for protonated GlyGlyAla are also available and nearly ready for publication at the time of this writing. Because the analysis is not yet complete, the detailed thermodynamic results are not included in Table 1, but the key results are shown in Figure 10c. Again the major channels match those of H⁺GGG and H⁺GAG, but moving the location of the methyl group changes the relative magnitudes of different products appreciably. In direct contrast to the H⁺GAG case, now the $[b_2]^+$ cross section is suppressed whereas that for the competing $[y_1+2H]^+$ channel is greatly enhanced. Now, the latter product is protonated alanine, H^+A at 90 m/z, and the $[b_2]^+$ product is again H⁺AMOx. Addition of the methyl group to the $[y_1+2H]^+$ product enhances its PA, making its formation nearly isoenergetic with that for H⁺AMOx. Because the magnitude of the [b₂]⁺ product cross section is smaller, so is the cross section for its subsequent dissociation product [a₂]⁺. Just as H⁺G dissociates by losing CO and H₂O to yield CH₂NH₂⁺, Figure 6, so does H⁺A dissociate to yield $CH_3CHNH_2^+$ at 44 m/z. The formation of $[y_2+2H]^+$ is also similar to that for H⁺GGG such that its dissociation product, [y₁+2H]⁺, again shows a second feature at higher energies. It can also be seen that the water loss channel yielding [b₃]⁺ and its subsequent decarbonylation product [a₃]⁺ have larger cross sections. This can be partly attributed to less competition with [b₂]⁺ but methylation near the C-terminus probably reduces the energy of the TTS leading to this product as well.

5.5 Protonated GlyProAla

Figure 10d shows TCID results for protonated GlyProAla, H⁺GPA, where now the cyclic proline residue has replaced the central glycine in GGA (Jones, Boles & Armentrout, 2020). These results are consistent with previous results obtained using metastable ion and single-energy CID studies (Grewal et al., 2004) but examine the kinetic energy dependence and include an additional three products. Our theoretical exploration of the mechanisms for dissociation parallel those for the tripeptides discussed above. As for these other protonated tripeptides, there are several primary

decomposition channels of H⁺GPA initiated by water loss, CO loss, and peptide bond cleavage (loss of A). As before, the water loss channel leads to [b₃]⁺ and further CO loss yields [a₃]⁺. Theoretically, the [b₃]⁺ ion is identified as 1-glycyl-2-pyrollo-4-methyl-5-oxazolone, H⁺GPAOx. This channel is relatively large compared with the other tripeptides because H⁺GPA has a *cis* peptide bond at proline, which facilitates the proton transfer from the N-terminus to the hydroxy group. In contrast, the cross section for [a₃]⁺ is relatively small compared to the cross section for its precursor [b₃]⁺. This may be attributable to a facile decomposition of the [a₃]⁺ product into the [b₂]⁺ product, as originally suggested by Allen et al. for other systems (Allen et al., 2008). This suggestion is consistent with theoretical calculations of the [a₃]⁺ decomposition energetics calculated in our study.

When H⁺GPA loses CO, it forms a proton bound dimer of CH₂NH and ProAla, an intermediate product that is not observed because theory indicates the formation of [y₂+2H]⁺, H⁺ProAla at 187 *m/z*, lies below the TTS leading to decarbonylation. This favorable energy occurs because the PA of ProAla is relatively high, a result of protonation on the tertiary nitrogen of the proline ring, whereas for GG, GA, and AG, this is only a secondary nitrogen. This enhanced PA also means that the competitive formation of [a₁]⁺ as a primary product is suppressed, explaining its small cross section compared to the other three tripeptides. Finally, no product corresponding to loss of CO and NH₃ is observed, again because the covalent C-N bond that would be needed occurs on the proline nitrogen, such that this site is a quaternary nitrogen in the purported product ion. This raises the energy of this product sufficiently that it can no longer compete with the other two channels dissociating through loose PSL TSs.

As for the other tripeptides, $[b_2]^+$ is the dominant product ion, in this case, identified as the bicyclic aminomethyl-1-pyrrolo-5-oxazolone, AMPOx⁺ at 155 m/z, in IRMPD studies by Wysocki and co-workers (Gucinski et al., 2013). Note there is no competitive formation of a $[y_1+2H]^+$ product, H⁺A at 90 m/z, which is because the charge of AMPOx⁺ is carried by a quaternary nitrogen that has no proton available for transfer to the Ala leaving group. Calculations also indicated that decomposition of $[y_2+2H]^+$ should preferentially form protonated pyrroline, H⁺(pyr) at 70 m/z,

whereas generation of $[y_1+2H]^+$ is a higher energy process. TCID studies of the $[b_2]^+$ ion formed in the source showed that this product decarbonylates to form $[a_2]^+$ at 127 m/z, and at higher energies decarbonylates again to form $H^+(pyr)$ in competition with $CH_2NH_2^+$, $[a_1]^+$ at 30 m/z. This latter decomposition is another example where the sequential dissociations cannot be modeled by our statistical analysis, as the decarbonylation is a TTS.

Possible formation of a H⁺DKP product instead of the oxazolone was also considered, but both theory and a number of experimental observations in the TCID results indicate that this alternate $[b_2]^+$ product is not formed, as also consistent with the IRMPD studies (Gucinski et al., 2013). This observation is notable because the ground structure of H⁺GPA has a *cis* orientation at the proline peptide bond. A *cis* orientation has been thought to be required for formation of the H⁺DKP $[b_2]^+$ product structure, whereas formation of the oxazolone requires a *trans* peptide bond (Paizs & Suhai, 2001a; Paizs & Suhai, 2002; Armentrout & Clark, 2012; Armentrout & Heaton, 2012a). For H⁺GPA, the TS between the *cis* and *trans* forms was calculated to lie about 80 kJ/mol above the lowest energy structure. This energy is well below that needed for H⁺GPA decomposition, 156 ± 4 kJ/mol for formation of $[b_3]^+$ and 206 ± 5 kJ/mol for formation of the predominant $[b_2]^+$ product, Table 1. We concluded that the *cis/trans* isomerization in H⁺GPA was necessary but not rate-limiting or influential in $[b_2]^+$ formation.

5.6 Thermodynamic Overview

Although the number of systems included in Table 1 is still relatively small, some trends in this thermochemistry can be noted. Generally, the loss of water from the C-terminus to form $[b_n]^+$ is the lowest energy process available, but experiment and theory show that this process is entropically disfavored. Subsequent decarbonylation to yield the $[a_n]^+$ fragment requires considerably more energy (88 – 117 kJ/mol). In contrast, cleavage of the peptide bond in a tripeptide to yield $[b_2]^+$ ions requires more energy (by 10 - 50 kJ/mol) but is the most efficient process. The threshold for this process is strongly dependent on the sequence, with addition of a methyl group decreasing the energy needed, and conversion to proline increasing the energy

needed. For the tripeptides studied here, [b₂]⁺ formation uniformly involves cyclization to form the oxazolone product. Studies investigating formation of competing H⁺DKP isomers are underway in our laboratory. Thresholds for the competing [y₁+2H]⁺ fragment do not vary widely, although this channel can be shut down entirely by the proline residue. The energies needed for [y₂+H]⁺ formation are also fairly constant with the competing [a₁]⁺ product requiring more energy. Notably, no [b₁]⁺ ions are observed in these systems as they readily undergo decarbonylation to yield [a₁]⁺ (Tsang & Harrison, 1976; Farrugia, O'Hair & Reid, 2001). More complicated sidechains are known to stabilize [b₁]⁺ by cyclization (Kulik & Heerma, 1988; Yalcin & Harrison, 1996; Tu & Harrison, 1998; Farrugia, O'Hair & Reid, 2001; Bythell et al., 2010).

6 PROTONATED DIPEPTIDES CONTAINING ASPARAGINE

One of the fastest spontaneous degradation processes of proteins is the deamidation of asparaginyl (Asn) residues (Robinson & Robinson, 2004). Under biological conditions, deamidation is believed to form a succinimide intermediate that can undergo hydrolysis, producing a combination of isoaspartate (iso-Asp, which puts an extra carbon in the backbone of the protein) and aspartate (Asp), typically found in a 3:1 ratio. These degradation effects have been shown to have major influences on biologically important factors such as modified protein function (Lindner & Helliger, 2001; Catterall et al., 2012) including the eye lens (Lampi et al., 1998; Lampi et al., 2014), and an altered potency of pharmaceuticals (Connolly et al., 2014). The formation of iso-Asp in this deamidation process has been linked to the onset and progression of Parkinson's and Alzheimer's disease (Nilsson, Driscoll & Raleigh, 2002; Robinson & Robinson, 2004).

Intriguingly, the rate of deamidation has been observed to vary appreciably (1.2 to >1000 days) among Gly-Yyy-Asn-Xxx-Gly sequences in solution-phase studies (Robinson & Robinson, 2001). The fastest deamidation rates were observed when Xxx was Gly, presumably because it introduces the least amount of steric hindrance interfering with succinimide ring formation. However, even though threonine (Thr) and valine (Val) are similar in size, the deamidation rate of the AsnVal sequence is more than five times that of AsnThr (Robinson & Robinson, 2001).

Likewise, AsnSer, even though bulkier than AsnAla, deamidates more rapidly. Thus, other factors beyond steric effects also influence deamidation rates. Our intent for these systems is to examine them on a fundamental level to determine (and quantify) specific interactions that play a significant role in hindering or accelerating the deamidation process. Such details are not easily ascertained in large scale solution phase studies.

6.1 Overview

Our interest in these systems began with our observations regarding Na⁺Asn (Heaton & Armentrout, 2008b), which we studied as part of a project to determine the sodium cation binding affinities of all the amino acids (summarized in Section 3.2). As detailed above, in addition to the loss of the intact Asn ligand, we also observed deamidation, Figure 3. We subsequently found that H⁺Asn (Heaton & Armentrout, 2009) would deamidate, Figure 8, and in both cases, the amino succinic anhydride (aSA) product (Figure 2) formed was related to the succinimide found biologically. To examine how the C-terminal side chain affects the kinetics and thermodynamics of the deamidation process, we have studied the sequence of protonated dipeptides of AsnXxx, where Xxx is Gly (Boles et al., 2016), Ala (Boles et al., 2018), Val (Kempkes et al., 2018), Ser (Boles et al., 2021), and Thr (Boles et al., 2019). In all of these studies, theoretical calculations were also performed to map out the reaction pathways and products.

Zero-pressure extrapolated cross sections for these five systems are shown in Figure 11. In all cases, the two main products are loss of water and loss of ammonia. It can be seen that the dehydration cross sections, which forms the $[b_2]^+$ ion, are fairly similar for all five systems, but those for deamidation vary appreciably, with H⁺AsnGly having the lowest threshold and largest cross section and that for H⁺AsnThr having the highest threshold and smallest cross section. Other minor products were also observed at higher energies, with the two main products being sequential ammonia loss (clearly a decomposition product of the primary deamidation reaction) and the $[a_1]^+$ ion, $H_2N=CHCH_2C(=O)NH_2^+$ (87 m/z), formed by loss of CO and Xxx and containing the amide side chain. Here, we focus on discussing the two primary channels.

6.2 Protonated AsnGly

One of the challenges for the GIBMS study of these systems is the close proximity of the two main products, differing by only one mass unit. In our study of the H⁺AsnGly system (Boles et al., 2016), we carefully considered whether we could operate under high mass resolution conditions and still maintain efficient collection of the products (needed to accurately determine the absolute cross sections required for thermodynamic analysis). This goal was checked by examining the decomposition using sustained off-resonance irradiation (SORI) CID in a Fourier transform ion cyclotron resonance mass spectrometer (FTICR MS) at Wayne State University in collaboration with Prof. M. T. Rodgers. Although the SORI-CID technique cannot measure absolute energies, it can reliably change the relative excitation of the cation such that the TCID results shown in Figure 11 could be quantitatively compared with the relative product magnitudes as a function of SORI power. The behavior observed in both experiments for all major products was very similar, with only minor differences for minor high-energy products, a consequence of single collision conditions in the GIBMS experiments versus multiple low-energy excitation in the FTICR study. This result lent confidence to the accuracy of the TCID cross sections.

As for the aliphatic peptides discussed above, the dehydration of $H^+AsnGly$ yields a $[b_2]^+$ ion having an oxazolone structure. The formation of this product is limited by a TTS shown in Figure 12, TS_O where R = H. Here, as a proton is transferred from the protonated side-chain carbonyl to the hydroxy group, the C-OH₂ bond cleaves, which is aided by ring-closure to form the five-membered oxazolone ring. For the deamidation reaction, we originally assumed that a succinimide product was formed, in analogy with the solution phase studies. An appropriate mechanism was determined with a rate-limiting TTS shown in Figure 13, TS_{N-Suc} for $H^+AsnXxx$ where R = H. Here, in a previous step, slightly lower in energy, a proton had been moved from the backbone imide to the side-chain amide nitrogen forming the NH₃ leaving group. In the TTS, the backbone nitrogen displaces the ammonia by forming the five-membered succinimide ring, a process stabilized by a hydrogen bond from NH₃ to the carbonyl of the carboxylic acid terminus.

As we were preparing our work for publication, we learned that an IRMPD study of H⁺AsnAla observed that the deamidation product had both a succinimide (Suc) structure and a furanone (Fur) structure (Kempkes et al., 2016). The alternate TTS leading to the latter product ion is also shown in Figure 13, TS_{N-Fur} for H⁺AsnXxx where R = H. Here, a previous step had transferred the proton from the N-terminus to the side-chain amide forming the NH₃ leaving group. Now, cleavage of the C-NH₃ bond is assisted by backside attack of the backbone carbonyl oxygen, forming the five-membered furanone ring, here stabilized by a hydrogen bond with the N-terminus. The final products were calculated to lie close in energy to the TTS (within 15 kJ/mol). Also TS_{N-Suc} and TS_{N-Fur} were calculated to have similar energies (within 20 kJ/mol), consistent with both pathways being accessible. Notably, deamination of the Suc product (yielding 156 *m/z*) lies much lower in energy than deamination of the Fur product, by 53 – 75 kJ/mol. Competitive modeling of the data was most consistent with formation of the Suc product at threshold with formation of Fur occurring at somewhat higher energies. This conclusion is also supported by the modeling of the 156 *m/z* product, which is consistent with NH₃ loss from Suc, but inconsistent with deamination of Fur.

6.3 Protonated AsnAla and AsnVal

Figure 11 shows that the decomposition of H⁺AsnAla parallels that for H⁺AsnGly, but the dehydration process is relatively larger in the former system. This result was supported by complementary SORI-CID studies (Boles et al., 2018). Mechanisms for H₂O and NH₃ loss parallel those for H⁺Gly in detail, with the TTSs involved shown in Figures 12 and 13, H⁺AsnXxx where R = CH₃; however, theory finds that the formation of Fur is favored over Suc. Modeling of the data yielded thresholds for dehydration and deamination that were consistent with oxazolone formation and Fur formation, but inconsistent with Suc formation, although this species could be formed at higher energies.

For H⁺AsnVal, the magnitude of the deamidation cross section continues to decrease compared to those for H⁺AsnGly and H⁺AsnAla, partly because the apparent threshold increases,

Figure 11 (Kempkes et al., 2018). Likewise, the dehydration channel has a higher apparent threshold, such that both reactions again compete in the threshold region. TSs again parallel those for the smaller aliphatic dipeptides, as shown in Figures 12 and 13, $H^+AsnXxx$ where $R = CH(CH_3)_2$. For this system, we collaborated with the Free Electron Lasers for Infrared eXperiments (FELIX) group to investigate the IRMPD of the reactants and products. These results showed that deamidation yielded the Fur product exclusively, and that the sequential NH_3 loss channel yielding $197 \, m/z$ also contained the Fur ring. These results are consistent with calculations that put the rate-limiting step for Suc formation $7-40 \, \text{kJ/mol}$ above that for Fur production.

6.4 Protonated AsnSer and AsnThr

TCID results for H⁺AsnSer (Boles et al., 2021) and H⁺AsnThr (Boles et al., 2019) are also shown in Figure 11. Clearly, the dehydration reaction becomes more favorable than deamidation in these systems compared to their aliphatic counterparts. IRMPD studies have shown that this is because a new channel for dehydration becomes available to protonated dipeptides containing hydroxy side chains, H⁺XxxSer and H⁺XxxThr (Oomens et al., 2020). The spectra definitively show that these systems form oxazolines rather than oxazolones, and that H⁺AsnSer also formed another minor species. An initial theoretical examination of the mechanisms for these dehydration reactions was consistent with these assignments. A more comprehensive examination of the pathways available for dehydration of H⁺AsnSer (Boles et al., 2021) showed that the reaction could proceed through two nearly isoenergetic tetrahedral intermediates that can be formed by proton transfer from the serine hydroxy group to either the carboxamide side chain or to the N-terminus, where the latter is the lowest energy step, TS_{O-Pre} in Figure 12. From the two tetrahedral intermediates, there were seven distinct pathways leading to dehydration, with the lowest being TS_{O-Tet} in Figure 12. For H⁺AsnThr, reinvestigated in (Boles et al., 2021), there are fewer pathways because of the extra methyl group, but the lowest energy pathway shown in Figure 12 remains the same. Now, theory shows that formation of the oxazoline has a lower energy pathway than formation of oxazolone, which is not observed experimentally in either H⁺AsnSer or H⁺AsnThr. For H⁺AsnSer, the minor species observed was initially thought to be a monoketopiperazine on the basis of this products low energy (Oomens et al., 2020). The more complete examination of the pathways for product generation (Boles et al., 2021) identified a protonated diketopiperazine (DKP) as a more likely product and one still consistent with the spectroscopic analysis of the dehydration product.

The mechanisms for the deamidation reactions are also affected by the hydroxy side chain. As shown in Figure 13, the pathway for Suc formation involves TS_{N-Suc} (H⁺AsnYyy) in which the incipient ammonia product is now stabilized by two hydrogen bonding interactions instead of just one in TS_{N-Suc} (H⁺AsnXxx). In one of these interactions, the side-chain replaces the carboxylic acid, and in the other, there is a new hydrogen bond with the N-terminal nitrogen. This latter interaction can occur because the protonated backbone carbonyl can now interact with the carboxylic acid instead of with the N-terminus. Clearly, the more extensive hydrogen bonding can stabilize the deamidation TS_{N-Suc}. In contrast, TS_{N-Fur} does not see such an increase in stabilization because the hydrogen bonding to NH₃ is the same for both TS_{N-Fur} transition states, Figure 13, although the amide nitrogen now forms a hydrogen bond with the side chain oxygen, rather than the carboxylic acid carbonyl. As a consequence of these changes, in H⁺AsnSer, IRMPD action spectroscopy shows that both Suc and Fur are formed, with the former dominating. This is also consistent with modeling of the TCID data, which was able to extract thresholds for both pathways, confirming that Suc formation is energetically favored. For H⁺AsnThr, IRMPD work shows exclusive Suc formation, even though several levels of theory suggest the Fur pathway should be energetically competitive; however, MP2 theory puts Suc formation 16 kJ/mol below that for Fur, consistent with the spectroscopic results.

6.5 Thermodynamic overview

Table 2 lists the thresholds for deamidation and dehydration measured for the five $H^{+}AsnXxx$ systems we have studied experimentally. It can be seen that the dehydration reactions are lower in energy in all cases. Although this conclusion seems evident from the data for Xxx = 1

Ser and Thr, the three aliphatic systems appear as though the two pathways should be more comparable. Our modeling demonstrates that the dehydration channel is entropically disfavored, which can be seen because the dehydration cross section is smaller at higher energies in all systems except H⁺AsnThr, where the thermodynamic difference between the two channels is the largest. This conclusion is consistent with the theoretical calculations, which indicate that the dehydration channel has a tighter rate-limiting TS. Table 2 shows that the experimental thresholds for deamidation of H⁺AsnXxx to form the Suc product do increase in accord with expectations from the solution phase rates (listed as the lifetimes, τ) for the same process in the pentapeptides. This correspondence can be seen more easily by converting these rates to approximate relative solutionphase activation energies, Ea, using the Arrhenius expression, $k = 1/\tau = A \exp(-Ea/k_BT)$, where k_B is Boltzmann's constant. (The values for Ea listed in Table 2 use T = 310 K (body temperature) and the pre-exponential factor $A = 10^{17} \text{ s}^{-1}$, chosen to reproduce the gas-phase experimental threshold energies.) Although the H⁺AsnVal system formed the Fur product exclusively, this is because the energy associated with Suc formation is much higher in this case, in accord with theory. Likewise, for H⁺AsnAla, Fur formation is favored according to theory, consistent with formation of this product at threshold.

In some respects, it is unfortunate that the alternative deamidation pathway of Fur formation is available in the gas phase (although analogous processes have been reported in solution, (Robinson & Robinson, 2004)), as it limits the comparisons that can be made with the more common succinimide pathway seen in solution phase studies. Theory can fill in the blanks, however, as the TSs for deamidation in all systems can be compared directly. Notably, theory and experiment agree reasonably well with mean absolute deviations for the data in Table 2 of 10 ± 7 and 8 ± 8 kJ/mol for B3LYP and MP2 theory, respectively. Qualitatively, the theoretical predictions for the rate-limiting deamidation steps are again parallel with the solution phase rates except perhaps for H⁺AsnThr, which would be expected to lie above H⁺AsnAla. Further, in agreement with the solution phase rates, addition of a hydroxy side chain clearly lowers the barrier for deamidation (compare Ala versus Ser and Thr versus Val). Theory shows that this is more than

steric effects and that the hydroxy side chain participates directly in helping to stabilize the ammonia leaving group. Further, the position of the side chain R group in TS_{N-Suc} (Figure 13), which is remote from where the ammonia is being lost and the ring is closing, indicates that inductive effects of the side chain might be influential rather than just steric effects.

We have speculated that the reason that solution phase studies do not observe the analogue of Fur formation may be because the amide carbonyl is more strongly involved in H-bonding interactions in condensed media, reducing its nucleophilicity and the likelihood of forming furanone structures. Further, solvation by water and peptide chain length could also play distinct roles in the deamidation of Asn residues in the condensed-phase.

7 CONCLUSIONS

In this review, our observations regarding cationized amino acids and small peptides as examined using GIBMS techniques have been summarized. When alkali cations are utilized, the decompositions are generally fairly simple, often associated with only loss of the intact ligand. As the binding strength increases, more substantial fragmentation processes occur and reach a maximum for lithiated species, where the bonding is sufficiently strong that other covalent bond cleavages compete with loss of the intact ligand. In contrast to the alkali cations, because a proton forms a covalent bond with biological molecules, the fragmentations observed for protonated species are extensive. By comparing the quantitative thresholds determined using TCID obtained by GIBMS with those calculated by theory, the product ion structures and, just as critically, the mechanisms for their formation can be identified. In general, reasonable agreement between our experiments and theory is obtained. For instance, for the data in Table 1, the mean absolute deviations (MADs) between experiment and theory are 13 ± 13 kJ/mol for MP2 calculations and 20 ± 15 kJ/mol for B3LYP. Likewise, for Table 2, the MADs are 8 ± 8 and 10 ± 7 kJ/mol, respectively. Such agreement validates the theoretical assignments for both mechanisms and product structures.

Just like structure identification using IRMPD, the assignments of product structures from TCID thresholds require the complementary use of high-level ab initio calculations. In contrast to IRMPD, which can only examine the products, TCID studies are also sensitive to the TSs that control product formation and therefore can be used to identify mechanisms. Indeed, even cursory examination of the TCID thresholds often allows tight versus loose TSs to be identified experimentally, without the input of theory, although the latter often validates these assignments. Notably, although the mechanisms for these decomposition reactions have been explored theoretically by many investigators for some time, previously there had been no means of verifying these pathways experimentally.

It can also be realized that the energetics of these reactions are more difficult to accurately predict by theory than structures (and thus, IR spectra). Ideally, it would be valuable to know which levels of theory are providing the highest quality and most accurate information. Although not discussed above, different levels of theory predict different ground structures, e.g., the lowest energy isomer of H⁺GGG is O-protonated according to B3LYP but N-protonated according to MP2. IRMPD action spectra have observed both species, and therefore cannot differentiate which is the ground state (Wu & McMahon, 2007). At present, TCID experiments on conformationally selected species should be able to measure the energy differences between different isomers. A recent example is the two protomers of para-amino benzoic acid (O- and N-protonated) (Demireva & Armentrout, 2021). More advanced techniques to provide such information for peptides is ongoing in my laboratory.

Finally, how can the results obtained in the studies reviewed here contribute to the overall analytical goals of more effective and comprehensive sequencing of proteins? It can be realized that the measurement of absolute reaction cross sections as a function of energy, $\sigma(E)$, provides platform-independent information on the dissociations observed. Knowledge of the energy-dependent cross sections should permit prediction of the mass spectrum for that system on any instrument (which would require knowing how that instrument energizes the molecules), i.e., along the lines of the MassKinetics software (Drahos & Vékey, 2001). In that regard, the cross sections

measured here should be useful to "train" theoretical approaches seeking to make exactly such predictions. As one cannot possibly hope to directly measure $\sigma(E)$ for all systems of interest, the expansion to other systems may be accomplished theoretically, but this is useful only for validated approaches. In addition, the results of the work reviewed here reveals many guidelines for what kinds of dissociation might be expected and how changing the cationizing agent or the peptide/protein structure might influence those observations. Continued work in this area should permit an ever-broadening set of results for comparison.

ACKNOWLEDGEMENT

I thank my students whose names appear in the references for their considerable contributions to the work reviewed here, my collaborators: G. Berden, J. Oomens, M. T. Rodgers, and M. J. van Stipdonk, and the reviewers, who made several useful suggestions. This work has been funded by the National Science Foundation, CHE-1954142.

Table 1. Threshold energies (kJ/mol) for various decompositions of protonated peptides ^a

Reactant	$[b_n]^+$ (-H ₂ O)	$[a_n]^+([b_n]^+\text{-CO})$	$\left[b_2\right]^+$	$[a_2]^+([b_2]^+-CO)$	$[y_2+2H]^+$	$[y_1+2H]^+(H^+G)$	$[a_1]^+ (CH_2NH_2^+)$
H^+G^b	160 (5) TTS ^c						140 (8) PSL
	132 / 144						137 / 137
H^+GG^{d}	138 (5) TTS	236 (13) PSL	138 (5) TTS	236 (13) TTS		191 (7) PSL	212 (6) PSL
	135 / 151	226 / 230	135 / 151	226 / 230		189 / 180	211 / 198
H⁺GGG e	136 (9) TTS	224 (12) TTS	171 (6) PSL	327 (6) TTS	220 (6) PSL	183 (7) PSL	247 (7) PSL
	111 / 132	227 / 237	169 / 153	295 / 285	186 / 174	189 / 182	242 / 241
H^+GAG^f	147 (12) TTS	264 (16) TTS	160 (14) PSL	273 (8) TTS	213 (16) PSL	191 (10) PSL	261 (17) PSL
	111 / 137	229 / 241	159 / 141	278 / 261	181 / 168	209 / 205	245 / 246
H^+GPA^g	156 (4) TTS	245 (13) TTS	206 (5) PSL	310 (10) TTS	203 (6) TTS		>295 (7) PSL
	144 / 148	245 / 228	209 / 160	312 / 268	197 / 164		308 / 265

^a Experimental values (uncertainties in parentheses) in roman with the type of transition state indicated: TTS – tight TS, PSL – phase space limit. Theoretical values are given in italics as calculated at the MP2(full)/B3LYP level of theory: Level/6-311+G(2d,2p)//B3LYP/6-311+G(d,p). Mean absolute deviations between experiment and theory are 13 (13) / 20 (15) kJ/mol. ^b (Armentrout, Heaton & Ye, 2011). ^c Loss of CO rather than H₂O. ^d (Armentrout & Heaton, 2012a; Armentrout & Heaton, 2012b). ^e (Mookherjee, Van Stipdonk & Armentrout, 2017). ^f (Mookherjee & Armentrout, 2019). ^g (Jones, Boles & Armentrout, 2020).

Table 2. Experimental and theoretical threshold energies (kJ/mol) for three reactions of H⁺AsnXxx dipeptides and the rate (days) of deamidation of GlyYyyAsnXxxGly pentapeptides determined in solution

reaction	Reactant	Exp. (kJ/mol)	MP2 (kJ/mol)	B3LYP (kJ/mol)	Sol'n rate (days) ^a	Sol'n E _a (kJ/mol)
Suc formation	H ⁺ AsnGly ^b	129 ± 6	133	151	1.2	131
	H ⁺ AsnSer ^c	131 ± 12	130	151	16	137
	H ⁺ AsnAla ^d		137	163	25	138
	H ⁺ AsnThr ^e	142 ± 6	127	150	46	140
	H ⁺ AsnVal ^f		145	172	253	144
Fur formation	H ⁺ AsnGly ^b		144	132		
	H ⁺ AsnSer ^c	145 ± 12	144	138		
	H ⁺ AsnAla ^d	123 ± 5	134	132		
	H ⁺ AsnThr ^e		143	137		
	H ⁺ AsnVal ^f	129 ± 5	129	132		
Dehydration	H ⁺ AsnGly ^b	117 ± 6	111	127		
	H ⁺ AsnSer ^c	104 ± 10	100	113		
	H ⁺ AsnAla ^d	103 ± 6	98	119		
	H ⁺ AsnThr ^e	117 ± 5	91	111		
	H ⁺ AsnVal ^f	114 ± 5	103	116		
MAD^g			8 ± 8	10 ± 7		

^a (Robinson & Robinson, 2001). ^b (Boles et al., 2016). ^c (Boles et al., 2021). ^d (Boles et al., 2018). ^e (Boles et al., 2019). ^f (Kempkes et al., 2018). ^g Mean absolute deviation from experimental values.

Figure Captions

- Figure 1. Zero-pressure extrapolated cross sections for CID of Li⁺Pro with Xe as a function of kinetic energy in the center-of-mass frame (lower x-axis) and the laboratory frame (upper x-axis). The inset shows the theoretical ground structure of the reactant complex. Adapted from (Mookherjee & Armentrout, 2014).
- Figure 2. Experimental versus theoretical bond energies (kJ/mol) of sodium cations to the Asx and Glx amino acids and their fragments associated with HX loss. Uncertainties for the theoretical values are taken from values calculated at B3LYP, B3P86, and MP2 levels of theory.
- Figure 3. Zero-pressure extrapolated cross sections for CID of Na⁺Asn with Xe as a function of kinetic energy in the center-of-mass frame. Solid lines show the best fit to the data using the model of eq 1 convoluted over the neutral and ion kinetic and internal energy distributions. Dashed lines show the model cross sections in the absence of experimental kinetic energy broadening for reactions with an internal energy of 0 K. The inset shows the theoretical ground structure of the reactant complex. Adapted from (Heaton & Armentrout, 2008b).
- Figure 4. Transition state structures for deamidation of H⁺Asn and Na⁺Asn yielding H⁺aSA and Na⁺aSA, respectively, calculated at the B3LYP/6-311+G(d,p) level of theory. Grey dashed lines show hydrogen bonds and black dashed lines show bonds being made or broken. Structures of 2-aminomethyl-5-oxazolone (AMOx) and 3-amino-5-imino-2-furanone.
- Figure 5. Zero-pressure extrapolated cross sections for CID of Na⁺GGG with Xe as a function of kinetic energy in the center-of-mass frame. The inset shows the theoretical ground structure of the reactant complex. Adapted from (Ye & Armentrout, 2008a).
- Figure 6. Zero-pressure extrapolated cross sections for CID of H⁺Gly with Xe as a function of kinetic energy in the center-of-mass frame (lower x-axis) and the laboratory frame (upper x-axis). Solid lines show the best fit to the data using the model of eq 1 convoluted over the neutral and ion kinetic and internal energy distributions. Dashed lines show the model cross sections in the absence of experimental kinetic energy broadening for reactions with an internal energy of 0 K. Numbers indicate the mass-to-charge ratio of all ionic species. The inset shows the theoretical ground structure of the reactant complex. Adapted from (Armentrout, Heaton & Ye, 2011).

Figure 7. Cross sections for CID of H⁺Cys with Xe as a function of kinetic energy in the center-of-mass frame (lower x-axis) and the laboratory frame (upper x-axis). Numbers indicate the mass-to-charge ratio of all ionic species. Open and closed symbols indicate primary and secondary reaction products, respectively. The inset shows the theoretical ground structure of the reactant complex. Adapted from (Armentrout & Stennett, 2014).

Figure 8. Cross sections for CID of H⁺Asn with Xe as a function of kinetic energy in the center-of-mass frame (lower x-axis) and the laboratory frame (upper x-axis). Numbers indicate the mass-to-charge ratio of all ionic species. Open and closed symbols indicate primary and secondary reaction products, respectively. The inset shows the theoretical ground structure of the reactant complex. Adapted from (Heaton & Armentrout, 2009).

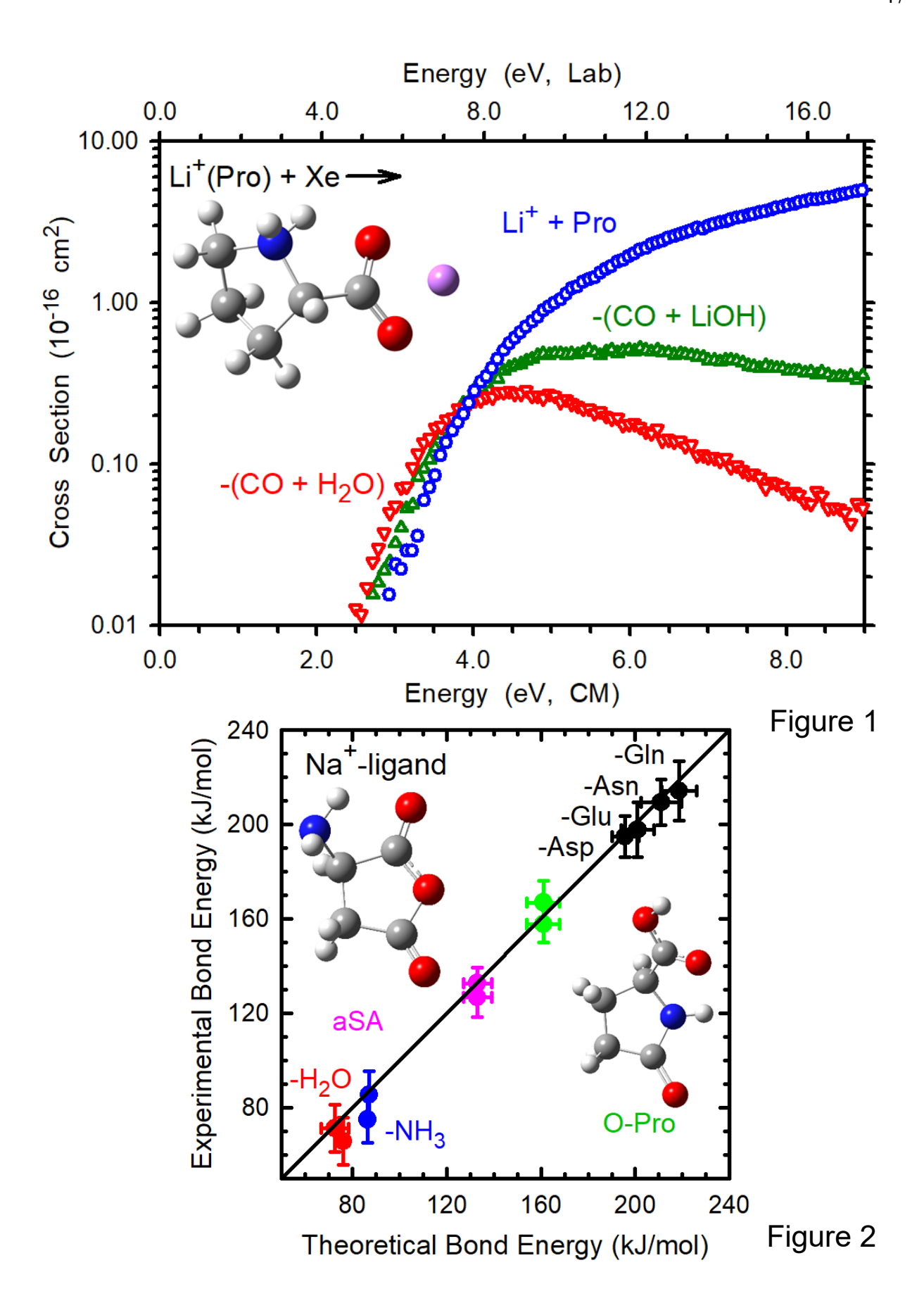
Figure 9. Cross sections for CID of H⁺GG with Xe as a function of kinetic energy in the center-of-mass frame (lower x-axis) and the laboratory frame (upper x-axis). Numbers indicate the mass-to-charge ratio of all ionic species. Open and closed symbols indicate primary and secondary reaction products, respectively. The inset shows the theoretical ground structure of the reactant complex. Adapted from (Armentrout & Heaton, 2012b).

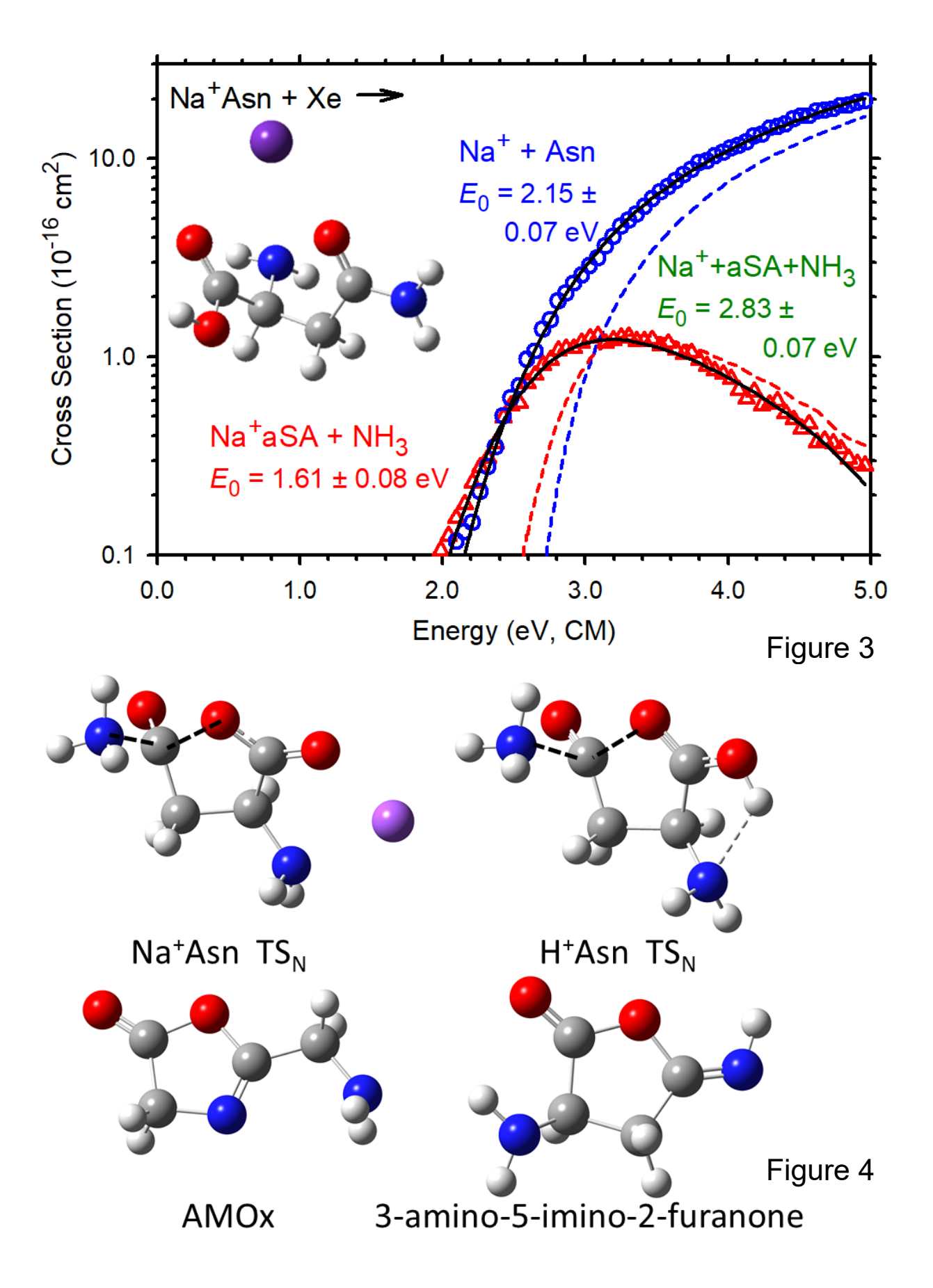
Figure 10. Cross sections for CID of H⁺GGG (part a), H⁺GAG (part b), H⁺GGA (part c), and H⁺GPA (part d) with Xe as a function of kinetic energy in the center-of-mass frame. Numbers indicate the mass-to-charge ratio of all ionic species. Open and closed symbols indicate primary and secondary reaction products, respectively. Adapted from (Mookherjee, Van Stipdonk & Armentrout, 2017; Mookherjee & Armentrout, 2019; Jones, Boles & Armentrout, 2020).

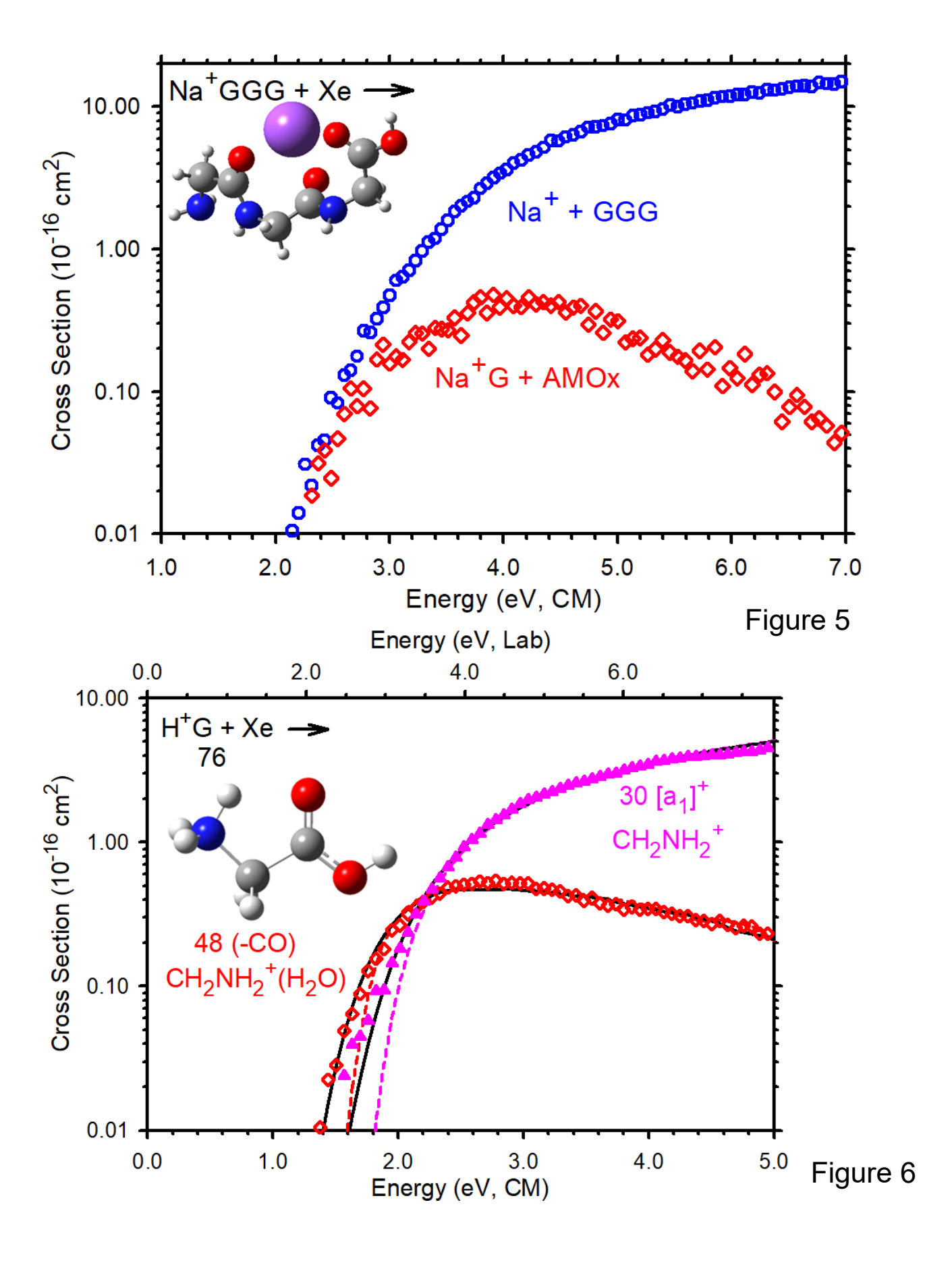
Figure 11. Zero-pressure extrapolated cross sections for CID of H⁺AsnXxx with Xe as a function of kinetic energy in the center-of-mass frame. Numbers indicate the mass-to-charge ratio of all ionic species. Adapted from (Boles et al., 2016; Boles et al., 2018; Kempkes et al., 2018; Boles et al., 2019; Boles et al., 2021).

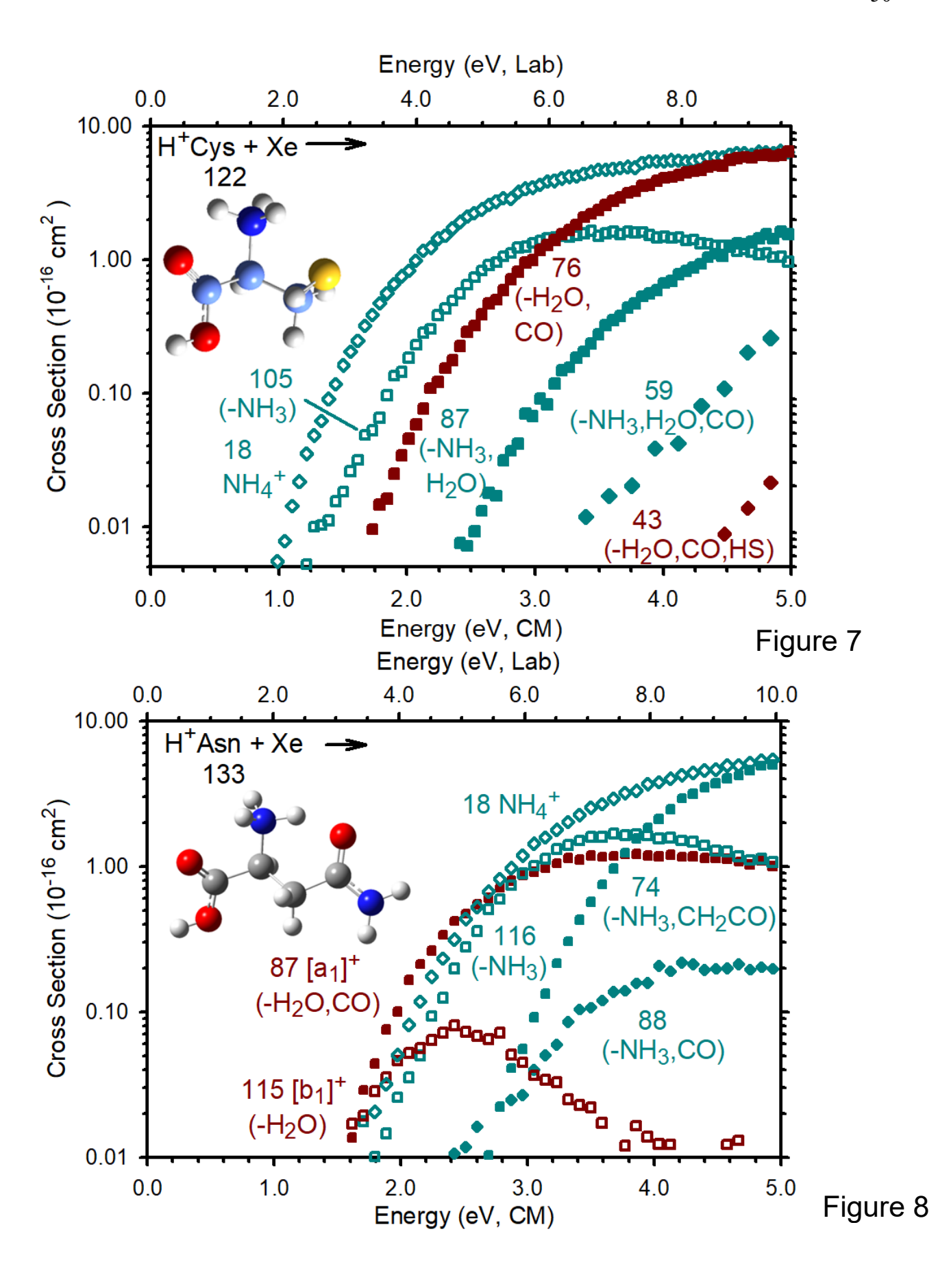
Figure 12. Transition state structures for dehydration of H⁺AsnXxx (Xxx = Gly, Ala, and Val) and Na⁺AsnYyy (Yyy = Ser and Thr) calculated at the B3LYP/6-311+G(d,p) level of theory. Grey dashed lines show hydrogen bonds and black dashed lines show bonds being made or broken.

Figure 13. Transition state structures for deamidation of $H^+AsnXxx$ (Xxx = Gly, Ala, and Val) and $Na^+AsnYyy$ (Yyy = Ser and Thr) forming a succinimide (TS_{N-Suc}) or furanone (TS_{N-Fur}) structure calculated at the B3LYP/6-311+G(d,p) level of theory. Grey dashed lines show hydrogen bonds and black dashed lines show bonds being made or broken.









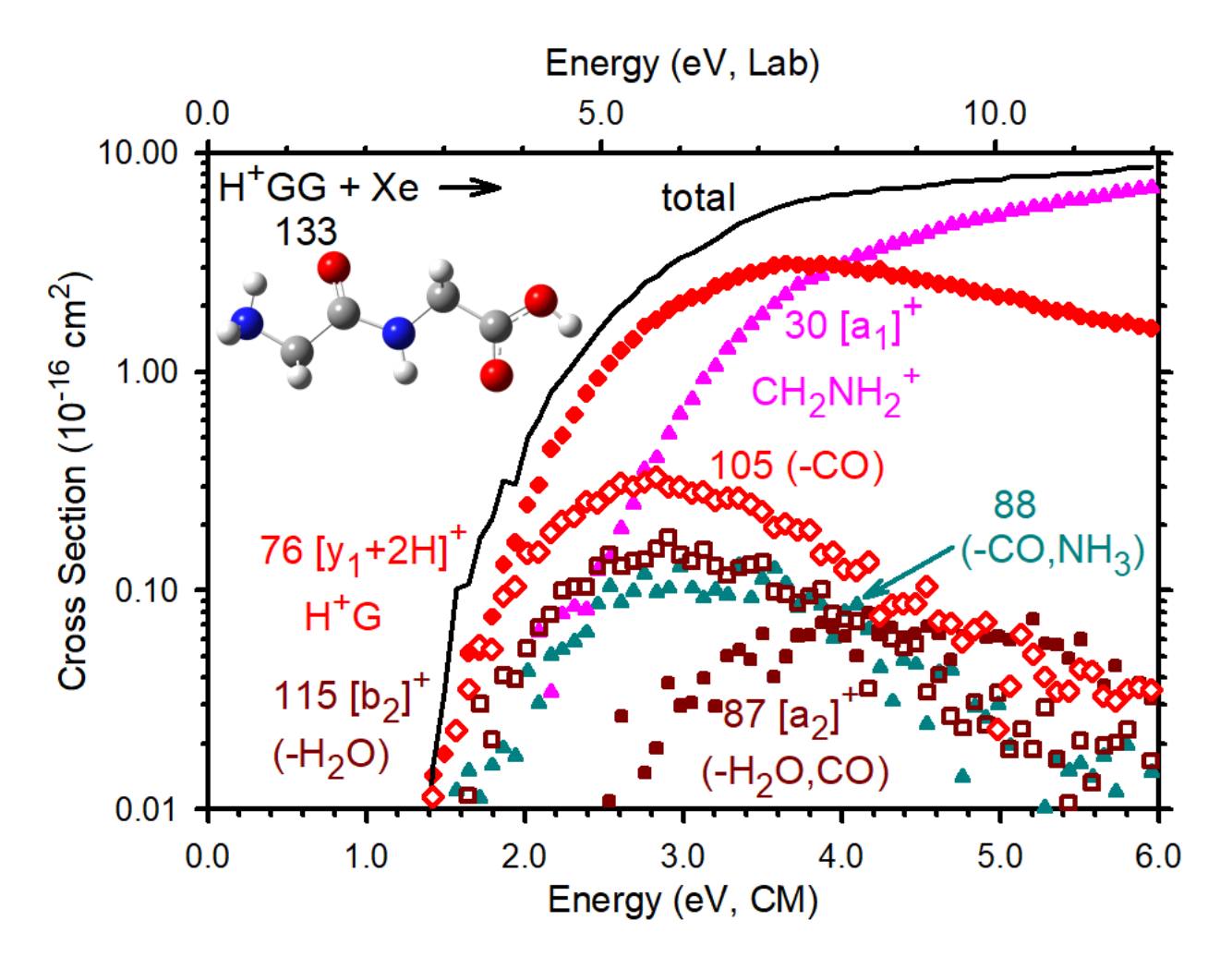
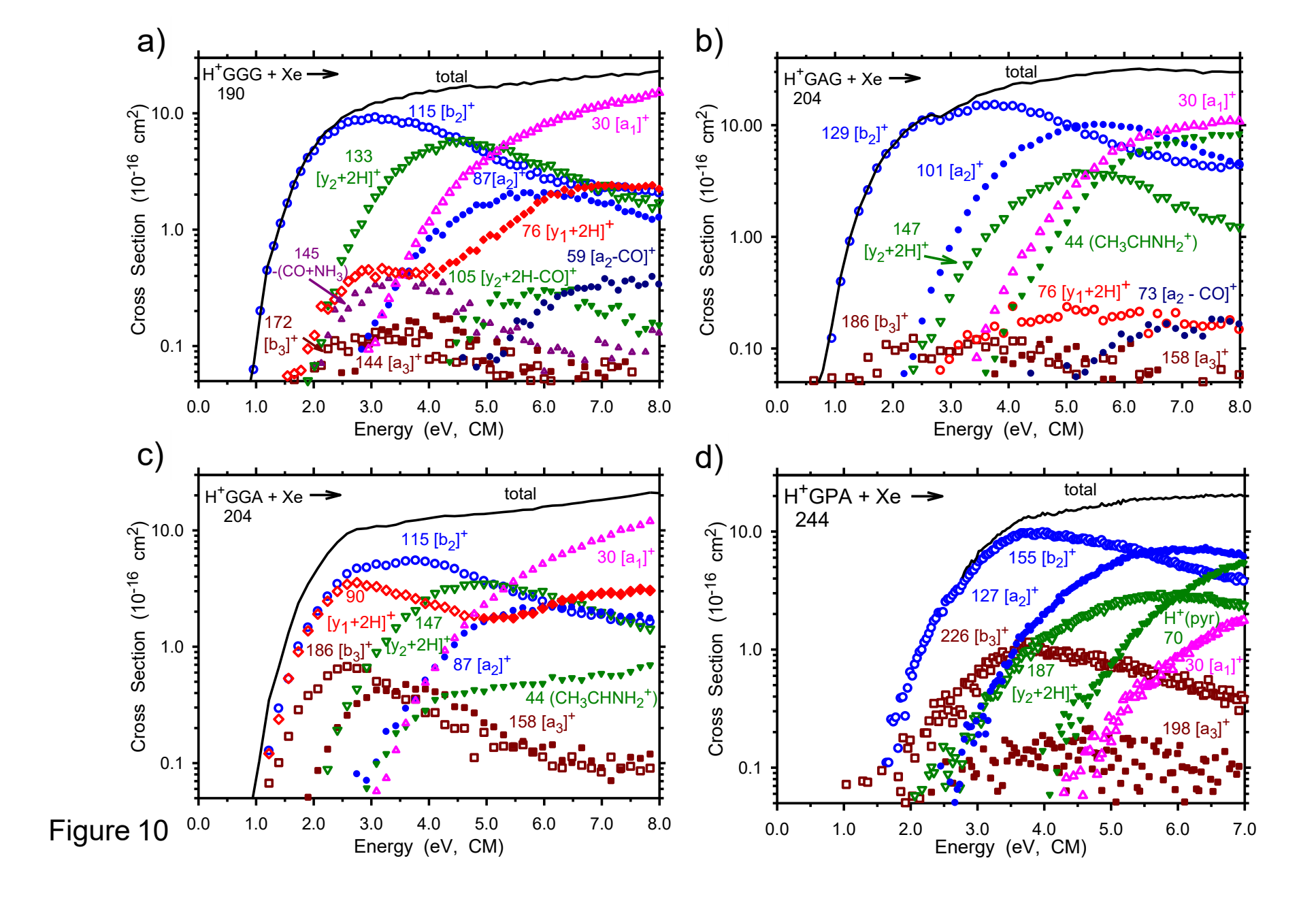


Figure 9



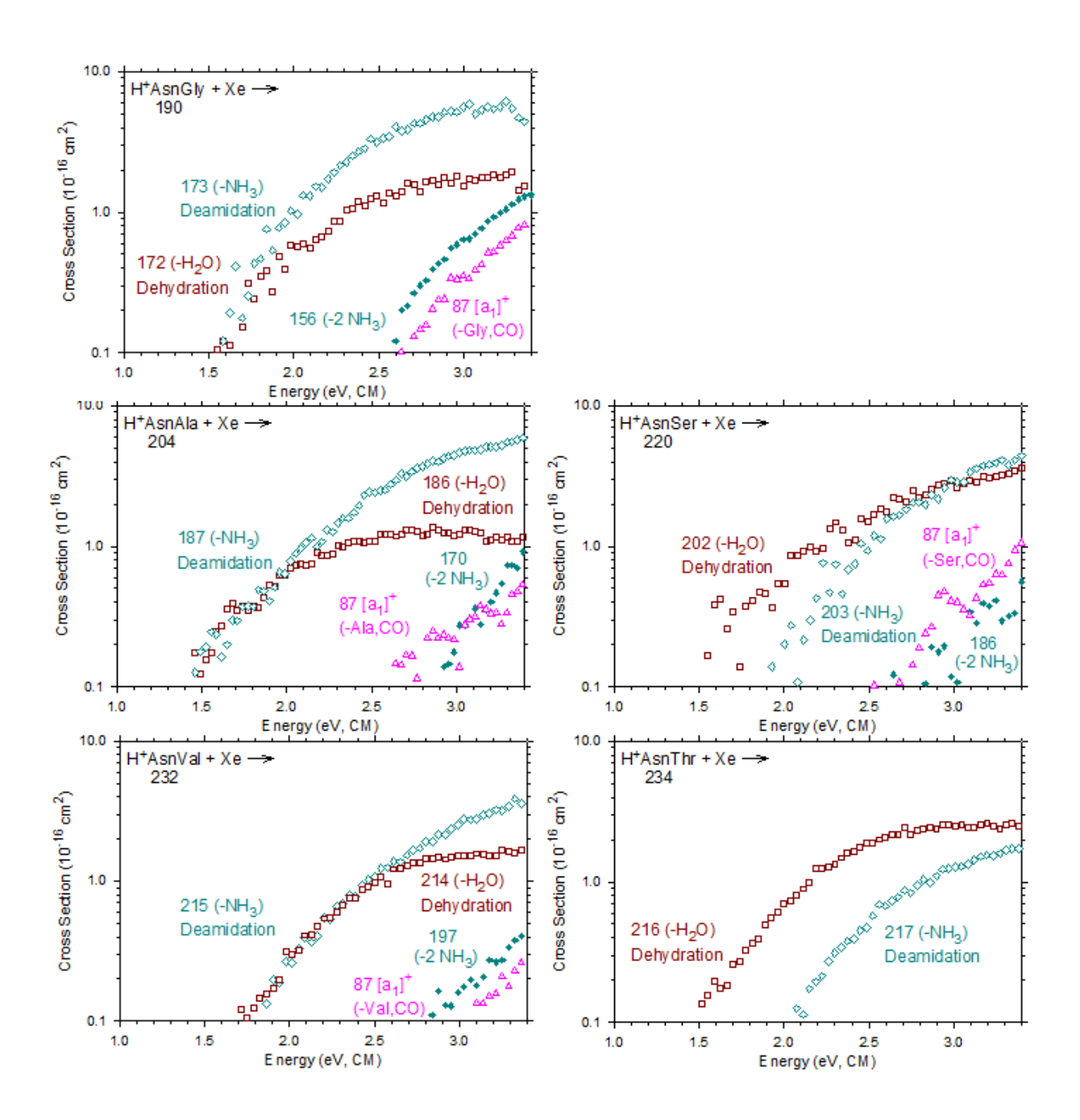


Figure 11

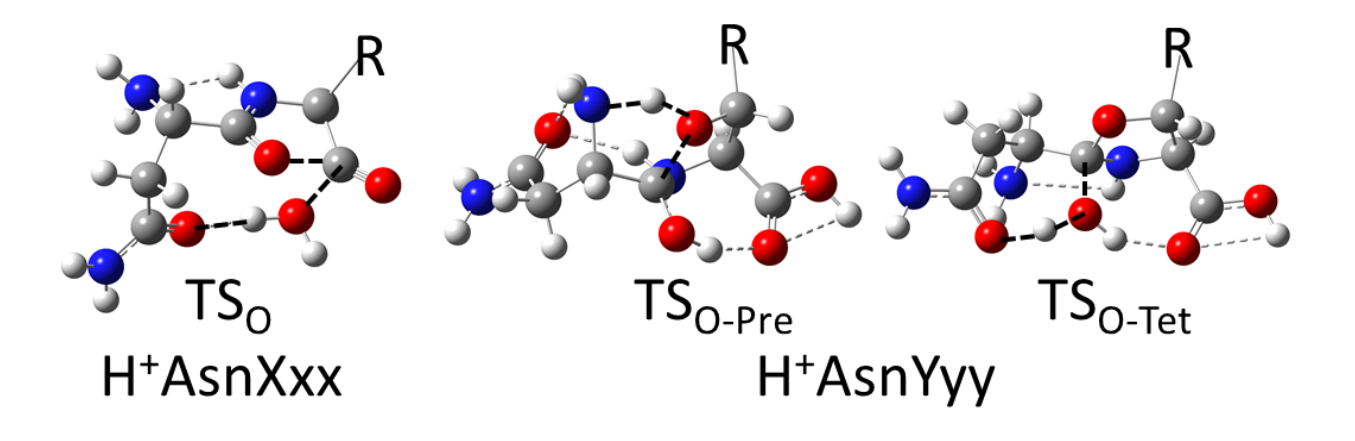


Figure 12

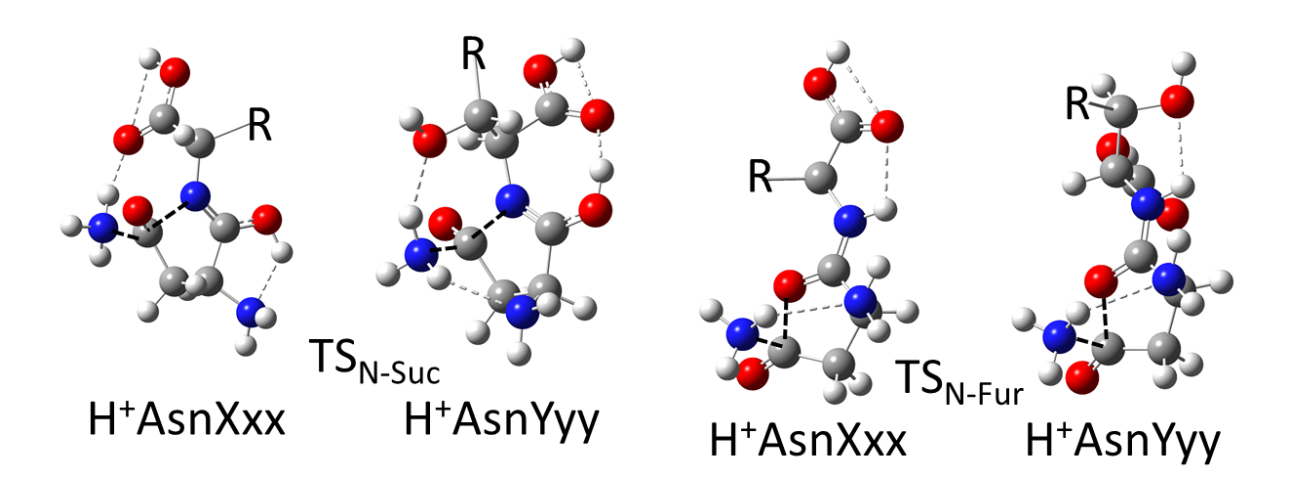


Figure 13

REFERENCES

Allen JM, Racine AH, Berman AM, Johnson JS, Bythell BJ, Paizs B, Glish GL. Why Are a₃ Ions Rarely Observed? 2008. J. Am. Soc. Mass Spectrom. 19:1764-1770.

Aribi HE, Orlova G, Hopkinson AC, Siu KWM. Gas-Phase Fragmentation Reactions of Protonated Aromatic Amino Acids: Concomitant and Consecutive Neutral Eliminations and Radical Cation Formations. 2004. J. Phys. Chem. A 108:3844-3853.

Armentrout PB. Not Just a Structural Tool: The Use of Guided Ion Beam Tandem Mass Spectrometry to Determine Thermochemistry. 2002. J. Am. Soc. Mass Spectrom. 13:419-434.

Armentrout PB. Statistical modeling of sequential collision-induced dissociation. 2007. J. Chem. Phys. 126:234302.

Armentrout PB, Armentrout EI, Clark AA, Cooper TE, Stennett EMS, Carl DR. An Experimental and Theoretical Study of Alkali Metal Cation Interactions with Cysteine. 2010a. J. Phys. Chem. B 114:3927-3937.

Armentrout PB, Chen Y, Rodgers MT. Metal Cation Dependence of Interactions with Amino Acids: Bond Energies of Cs⁺ to Gly, Pro, Ser, Thr, and Cys. 2012. J. Phys. Chem. A 116:3989-3999.

Armentrout PB, Citir M, Chen Y, Rodgers MT. Thermochemistry of Alkali Metal Cation Interactions with Histidine: Influence of the Side-Chain. 2012. J. Phys. Chem. A 116:11823-11832.

Armentrout PB, Clark AA. The Simplest b₂⁺ Ion: Determining Its Structure from Its Energetics by a Direct Comparison of the Threshold Collision-induced Dissociation of Protonated Oxazolone and Diketopiperazine. 2012. Int. J. Mass Spectrom. 316-318:182–191.

Armentrout PB, Gabriel A, Moision RM. An Experimental and Theoretical Study of Alkali Metal Cation/Methionine Interactions. 2009. Int. J. Mass Spectrom. 283:56-68.

Armentrout PB, Heaton AL. Thermodynamics and Mechanisms of Protonated Diglycine Decomposition: A Computational Study. 2012a. J. Am. Soc. Mass Spectrom. 23:621-631.

Armentrout PB, Heaton AL. Thermodynamics and Mechanisms of Protonated Diglycine Decomposition: A Guided Ion Beam Study. 2012b. J. Am. Soc. Mass Spectrom. 23:632-643.

Armentrout PB, Heaton AL, Ye SJ. Thermodynamics and Mechanisms for Decomposition of Protonated Glycine and Its Protonated Dimer. 2011. J. Phys. Chem. A 115:11144-11155.

Armentrout PB, Rodgers MT, Oomens J, Steill JD. Infrared Multiphoton Dissociation Spectroscopy of Cationized Serine: Effects of Alkali-Metal Cation Size on Gas-Phase Conformation. 2008. J. Phys. Chem. A 112:2248-2257.

Armentrout PB, Stennett EMS. Thermodynamics and Mechanism of Protonated Cysteine Decomposition: A Guided Ion Beam and Computational Study. 2014. J. Am. Soc. Mass Spectrom. 25:512-523.

Armentrout PB, Yang B, Rodgers MT. Metal Cation Dependence of Interactions with Amino Acids: Bond Energies of Rb⁺ and Cs⁺ to Met, Phe, Tyr, and Trp. 2013. J. Phys. Chem. B 117:3771-3781.

Armentrout PB, Yang B, Rodgers MT. Metal Cation Dependence of Interactions with Amino Acids: Bond Dissociation Energies of Rb⁺ and Cs⁺ to the Acidic Amino Acids and Their Amide Derivatives. 2014. J. Phys. Chem. B 118:4300–4314.

Armentrout PB, Ye SJ, Gabriel A, Moision RM. Energetics and Mechanism for the Deamination of Lithiated Cysteine. 2010b. J. Phys. Chem. B 114:3938-3949.

Balta B, Aviyente V, Lifshitz C. Elimination of Water from the Carboxyl Group of GlyGlyH⁺ 2003. J. Am. Soc. Mass Spectrom. 14:1192-1203.

Becke AD. Density-functional Thermochemistry. III. The Role of Exact Exchange. 1993. J. Chem. Phys. 98:5648-5652.

Begley DJ. The blood-brain barrier: principles for targeting peptides and drugs to the central nervous system. 1996. J. Pharm. Pharmacol. 48:136-146.

Beranova S, Cai J, Wesdemiotis CJ. Unimolecular Chemistry of Protonated Glycine and Its Neutralized Form in the Gas Phase. 1995. J. Am. Chem. Soc. 117:9492-9501.

- Beyer TS, Swinehart DF. Number of Multiply-Restricted Partitions. 1973. Commun. ACM 16:379.
- Bojesen G, Breindahl T, Andersen UN. On the Sodium and Lithium Ion Affinities of Some α-Amino Acids. 1993. Org. Mass Spectrom. 28:1448-1452.
- Boles GC, Kempkes LJM, Martens J, Berden G, Oomens J, Armentrout PB. Ion Spectroscopy and Guided Ion Beam Studies of Protonated Asparaginyl-Threonine Decomposition: Influence of a Hydroxyl Containing C-Terminal Residue on Deamidation Processes. 2019. Int. J. Mass Spectrom. 442:64-82.
- Boles GC, Kempkes LJM, Martens J, Berden G, Oomens J, Armentrout PB. Influence of a Hydroxyl Group on the Deamidation and Dehydration Reactions of Protonated Asparagine-Serine Investigated by Combined Spectroscopic, Guided Ion Beam, and Theoretical Approaches. 2021. J. Am. Soc. Mass Spectrom. 32:786-805.
- Boles GC, Wu RR, Rodgers MT, Armentrout PB. Thermodynamics and Mechanisms of Protonated Asparaginyl-Glycine Decomposition. 2016. J. Phys. Chem. B 120:6525–6545.
- Boles GC, Wu RR, Rodgers MT, Armentrout PB. Protonated Asparaginyl-Alanine Decomposition: a TCID, SORI-CID, and Computational Analysis. 2018. J. Am. Soc. Mass Spectrom. 29:2341-2359.
- Bourcier S, Chia RX, Bimbong RNB, Bouchoux G. Gas-phase lithium cation affinity of glycine. 2015. Eur. J. Mass Spectrom. 21:149-159.
- Bowman VN, Heaton AL, Armentrout PB. Metal Cation Dependence of Interactions with Amino Acids: Bond Energies of Rb⁺ to Gly, Ser, Thr, and Pro. 2010. J. Phys. Chem. B 114:4107-4114.
- Burlet O, Orkiszewski RS, Ballard KD, Gaskell SJ. Charge promotion of low-energy fragmentations of peptide ions. 1992. Rapid Commun. Mass Spectrom. 6:658-662.
- Bush MF, Forbes MW, Jockusch RA, Oomens J, Polfer NC, Saykally RJ, Williams ER. Infrared Spectroscopy of Cationized Lysine and ε-N-methyllysine in the Gas Phase: Effects of Alkali-Metal Ion Size and Proton Affinity on Zwitterion Stability. 2007a. J. Phys. Chem. A 111:7753-7760.
- Bush MF, O'Brien JT, Prell JS, Saykally RJ, Williams ER. Infrared Spectroscopy of Cationized Arginine in the Gas Phase: Direct Evidence for the Transition from Nonzwitterionic to Zwitterionic Structure. 2007b. J. Am. Chem. Soc. 129:1612-1622.
- Bush MF, Oomens J, Saykally RJ, Williams ER. Alkali Metal Ion Binding to Glutamine and Glutamine Derivatives Investigated by Infrared Action Spectroscopy and Theory. 2008. J. Phys. Chem. A 112:8578-8584.
- Bush MF, Oomens J, Williams ER. Proton Affinity and Zwitterion Stability: New Results from Infrared Spectroscopy and Theory of Cationized Lysine and Analogues in the Gas Phase. 2009. J. Phys. Chem. A 113:431-438.
- Bythell BJ, Barofsky DF, Pingitore F, Polce MJ, Wang P, Wesdemiotis C, Paizs B. Backbone cleavages and sequential loss of carbon monoxide and ammonia from protonated AGG: A combined tandem mass spectrometry, isotope labeling, and theoretical study. 2007. J. Am. Soc. Mass Spectrom. 18:1291-1303.
- Bythell BJ, Csonka IP, Suhai S, Barofsky DF, Paizs B. Gas-Phase Structure and Fragmentation Pathways of Singly Protonated Peptides with N-Terminal Arginine. 2010. J. Phys. Chem. B 114:15092-15105.
- Bythell BJ, Maitre P, Paizs B. Cyclization and Rearrangement Reactions of a_n Fragment Ions of Protonated Peptides. 2010. J. Am. Chem. Soc. 132:14766-14779.
- Carl DR, Chatterjee BK, Armentrout PB. Threshold Collision-induced Dissociation of $Sr^{2+}(H_2O)_x$ Complexes (x = 1 6): An Experimental and Theoretical Investigation of the Complete Inner Shell Hydration Energies of Sr^{2+} . 2010. J. Chem. Phys. 132:044303.
- Carl DR, Cooper TE, Oomens J, Steill JD, Armentrout PB. Infrared Multiple Photon Dissociation Spectroscopy of Cationized Methionine: Effects of Alkali-Metal Cation Size on Gas-Phase Conformation. 2010. Phys. Chem. Chem. Phys. 12:3384-3398.
- Carl DR, Moision RM, Armentrout PB. Binding Energies for the Inner Hydration Shells of Ca²⁺: An Experimental and Theoretical Investigation of Ca²⁺(H₂O)_x Complexes (x = 5 9). 2007. Int. J. Mass Spectrom. 265:308-325.

Carl DR, Moision RM, Armentrout PB. In-source Fragmentation Technique for the Production of Thermalized Ions. 2009. J. Am. Soc. Mass Spectrom. 20:2312-2317.

Carpenter JE, McNary CP, Furin A, Sweeney AF, Armentrout PB. How Hot are Your Ions Really? A Threshold Collision-Induced Dissociation Study of Substituted Benzylpyridinium "Thermometer" Ions. 2017. J. Am. Soc. Mass Spectrom. 28:1876-1888.

Catterall JB, Hsueh MF, Stabler TV, McCudden CR, Bolognesi M, Zura R, Jordan JM, Renner JB, Feng S, Kraus VB. Protein Modification by Deamidation Indicates Variations in Joint Extracellular Matrix Turnover. 2012. J. Biol. Chem. 287:4640-4651.

Cerda BA, Hoyau S, Ohanessian G, Wesdemiotis C. Na⁺ Binding to Cyclic and Linear Dipeptides. Binding Energies, Entropies of Na⁺ Complexation, and Attachment Sites from the Dissociation of Na⁺-bound Heterodimers and Ab Initio Calculations. 1998. J. Am. Chem. Soc. 120:2437-2448.

Citir M, Hinton CS, Oomens J, Steill JD, Armentrout PB. Infrared Multiple Photon Dissociation Spectroscopy of Cationized Histidine: Effects of Metal Cation Size on Gas-Phase Conformation. 2012. J. Phys. Chem. A 116:1532-1541.

Citir M, Stennett EMS, Oomens J, Steill JD, Rodgers MT, Armentrout PB. Infrared Multiple Photon Dissociation Spectroscopy of Cationized Cysteine: Effects of Metal Cation Size on Gas-Phase Conformation. 2010. Int. J. Mass Spectrom. 297:9-17.

Clark AA, Yang B, Rodgers MT, Armentrout PB. Experimental and Computational Study of the Group 1 Metal Cation Chelates with Lysine: Bond Dissociation Energies, Structures, and Structural Trends. 2019. J. Phys. Chem. B 123:1983-1997.

Connolly BD, Tran B, Moore JM, Sharma VK, Kosky A. Specific Catalysis of Asparaginyl Deamidation by Carboxylic Acids: Kinetic, Thermodynamic, and Quantitative Structure-Property Relationship Analyses. 2014. Mol. Pharm. 11:1345-1358.

Cox KA, Gaskell, S.J., Morris, M., Whiting, A. Role of the site of protonation in the low-energy decompositions of gas-phase peptide ions. 1996. J. Am. Soc. Mass Spectrom. 7:522-531.

Dalleska NF, Honma K, Armentrout PB. Stepwise Solvation Enthalpies of Protonated Water Clusters: Collision Induced Dissociation as an Alternative to Equilibrium Studies. 1993. J. Am. Chem. Soc. 115:12125-12131.

Daly NR. Scintillation Type Mass Spectrometer Ion Detector. 1960. Rev. Sci. Instrum. 31:264-267.

Demireva M, Armentrout PB. Relative Energetics of the Gas Phase Protomers of p Aminobenzoic Acid and the Effect of Protonation Site on Fragmentation. 2021. J. Phys. Chem. A 125:2849-2865. Dongré AR, Jones JL, Somogyi A, Wysocki VH. Influence of Peptide Composition, Gas-Phase Basicity, and Chemical Modification on Fragmentation Efficiency: Evidence for the Mobile Proton Model. 1996. J. Am. Chem. Soc. 118:8365-8374.

Dookeran NN, Yalcin T, Harrison AG. Fragmentation Reactions of Protonated α -Amino Acids. 1996. J. Mass Spectrometry 31:500-508.

Drahos L, Vékey K. MassKinetics: a theoretical model of mass spectra incorporating physical processes, reaction kinetics and mathematical descriptions. 2001. J. Mass Spectrom. 36:237-263. Drayss MK, Armentrout PB, Oomens J, Schäfer M. IR Spectroscopy of Cationized Aliphatic Amino Acids: Stability of Charge-solvated Structure Increases with Metal Cation Size. 2010. Int. J. Mass Spectrom. 297:18–27.

Drayss MK, Blunk D, Oomens J, Schäfer M. Infrared Multiple Photon Dissociation Spectroscopy of Potassiated Proline. 2008. J. Phys Chem. A 112:11972-11974.

Dunbar RC, Steill JD, Oomens J. Cationized phenylalanine conformations characterized by IRMPD and computation for singly and doubly charged ions. 2010. Phys. Chem. Chem. Phys. 12:13383-13393.

El Aribi H, Rodriquez CF, Almeida DRP, Ling Y, Mak WW-N, Hopkinson AC, Siu KWM. Elucidation of Fragmentation Mechanisms of Protonated Peptide Ions and Their Products: A Case Study on Glycylglycine Using Density Functional Theory and Threshold Collision-Induced Dissociation. 2003. J. Am. Chem. Soc. 125:9229-9236.

Ervin KM, Armentrout PB. Translational Energy Dependence of $Ar^+ + XY \rightarrow ArX^+ + Y$ (XY = H₂, D₂, HD) from Thermal to 30 eV c.m. 1985. J. Chem. Phys. 83:166-189.

Farrugia JM, O'Hair RAJ, Reid GE. Do all b2 ions have oxazolone structures? Multistage mass spectrometry and ab initio studies on protonated N-acyl amino acid methyl ester model systems3†Part 28 of the series "Gas Phase Ion Chemistry of Biomolecules."33Dedicated to Professor Nibbering on the occasion of his retirement and in recognition of his many seminal contributions to the physical organic chemistry of gas phase ions. 2001. Int. J. Mass Spectrom. 210-211:71-87.

Feng WY, Gronert S, Lebrilla CB. Lithium and Sodium Ion Binding Energies on N-Acetyl and N-Glycyl Amino Acids. 1999. J. Am. Chem. Soc. 121:1365-1371.

Forbes MW, Bush MF, Polfer NC, Oomens J, Dunbar RC, Williams ER, Jockusch RA. Infrared Spectroscopy of Arginine Cation Complexes: Direct Observation of Gas-Phase Zwitterions. 2007. J. Phys. Chem. A 111:11759-11770.

Gapeev A, Dunbar RC. Cation-Pi Interactions and the Gas-Phase Thermochemistry of the Na⁺/Phenylalanine Complex. 2001. J. Am. Chem. Soc. 123:8360-8365.

Gapeev A, Dunbar RC. Na⁺ Affinities of Gas-phase Amino Acids by Ligand Exchange Equilibrium. 2003. Int. J. Mass Spectrom. 228:825-839.

Gerlich D. 1992. Inhomogeneous rf Fields: A Versatile Tool for the Study of Processes with Slow Ions. In: Ng C-Y, Baer M, Editors. Adv. Chem. Phys.: Wiley. p 1-176.

Gilbert RG, Smith SC. 1990. Theory of Unimolecular and Recombination Reactions. London: Blackwell Scientific.

Grewal RN, El Aribi H, Harrison AG, Siu KWM, Hopkinson AC. Fragmentation of Protonated Tripeptides: The Proline Effect Revisited. 2004. J. Phys. Chem. B 108:4899-4908.

Gucinski AC, Chamot-Rooke J, Steinmetz V, Somogyi A, Wysocki VH. Influence of N-terminal Residue Composition on the Structure of Proline-Containing b₂⁺ Ions. 2013. J. Phys. Chem. A 117:1291–1298.

Heaton AL, Armentrout PB. Experimental and Theoretical Studies of Potassium Cation Interactions with the Acidic Amino Acids and Their Amide Derivatives. 2008a. J. Phys. Chem. B 112:12056–12065.

Heaton AL, Armentrout PB. Thermodynamics and Mechanism of the Deamidation of Sodium-Bound Asparagine. 2008b. J. Am. Chem. Soc. 130:10227-10232.

Heaton AL, Armentrout PB. Thermodynamics and Mechanism of Protonated Asparagine Decomposition. 2009. J. Am. Soc. Mass Spectrom. 20:852-866.

Heaton AL, Bowman VN, Oomens J, Steill JD, Armentrout PB. Infrared Multiple Photon Dissociation Spectroscopy of Cationized Asparagine: Effects of Metal Cation Size on Gas-Phase Conformation. 2009. J. Phys. Chem. A 113:5519-5530.

Heaton AL, Moision RM, Armentrout PB. Experimental and Theoretical Studies of Sodium Cation Interactions with the Acidic Amino Acids and Their Amide Derivatives. 2008. J. Phys. Chem. A 112:3319-3327.

Heaton AL, Ye SJ, Armentrout PB. Experimental and Theoretical Studies of Sodium Cation Complexes of the Deamidation and Dehydration Products of Asparagine, Glutamine, Aspartic Acid, and Glutamic Acid. 2008. J. Phys. Chem. A 112:3328-3338.

Hehre WJ. Ab initio molecular orbital theory. 1976. Acc. Chem. Res. 9:399-406.

Hughes J, Smith TW, Kosterlitz HW, Fothergill LA, Morgan BA, Morris HR. Identification of two related pentapeptides from the brain with potent opiate agonist activity. 1975. Nature 258:577-580.

Jones RM, Boles GC, Armentrout PB. Cis-trans isomerization is not rate determining for b2 ion structures: A guided ion beam and computational study of the decomposition of H+(GlyProAla). 2020. Int. J. Mass Spectrom. 458:116434.

Kapota C, Lemaire J, Maitre P, Ohanessian G. Vibrational Signature of Charge Solvation vs Salt Bridge Isomers of Sodiated Amino Acids in the Gas Phase. 2004. J. Am. Chem. Soc. 126:1836-1842.

Kempkes LJM, Boles GC, Martens J, Berden G, Armentrout PB, Oomens J. Deamidation of Protonated Asparagine–Valine Investigated by a Combined Spectroscopic, Guided Ion Beam, and Theoretical Study. 2018. J. Phys. Chem. A 122:2424-2436.

Kempkes LJM, Martens JK, Grzetic J, Berden G, Oomens J. Deamidation Reactions of Protonated Asparagine and Glutamine Investigated by Ion Spectroscopy. 2016. Rapid Commun. Mass Spectrom. 30:483-490.

Khan FA, Clemmer DE, Schultz RH, Armentrout PB. Sequential Bond Energies of $Cr(CO)_x^+$, x = 1 - 6. 1993. J. Phys. Chem. 97:7978-7987.

Kim T, Tolmachev AV, Harkewicz R, Prior DC, Anderson G, Udseth HR, Smith RD, Bailey TH, Rakov S, Futrell JH. Design and Implementation of a New Electrodynamic Ion Funnel. 2000. Anal. Chem 72:2247-2255.

Kish MM, Ohanessian G, Wesdemiotis C. The Na⁺ Affinities of α-Amino Acids: Side-chain Substituent Effects. 2003. Int. J. Mass Spectrom. 227:509-524.

Kish MM, Wesdemiotis C, Ohanessian G. The Sodium Ion Affinity of Glycylglycine. 2004. J. Phys. Chem. B 108:3086-3091.

Klassen JS, Anderson SG, Blades AT, Kebarle P. Reaction Enthalpies for $M^+L = M^+ + L$, Where $M^+ = Na^+$ and K^+ and L = Acetamide, N-methylacetamide, N,N-dimethylacetamide, Glycine, and Glycylglycine, from Determinations of the Collision-induced Dissociation Thresholds. 1996. J. Phys. Chem. 100:14218-14227.

Klassen JS, Kebarle P. Collision-induced Dissociation Threshold Energies of Protonated Glycine, Glycinamide, and Some Related Small Peptides and Peptide Amino Amides. 1997. J. Am. Chem. Soc. 119:6552-6563.

Kulik W, Heerma W. A study of the positive and negative ion fast atom bombardment mass spectra of alpha-amino acids. 1988. Biomedical & environmental mass spectrometry 15:419-427.

Lampi KJ, Ma Z, Hanson SRA, Azuma M, Shih M, Shearer TR, Smith DL, Smith JB, David LL. Age-related Changes in Human Lens Crystallins Identified by Two-dimensional Electrophoresis and Mass Spectrometry. 1998. Exp. Eye Res. 67:31-43.

Lampi KJ, Wilmarth PA, Murray MR, David LL. Lens β-crystallins: The role of deamidation and related modifications in aging and cataract. 2014. Progress in Biophysics and Molecular Biology 115:21-31.

Lee C, Yang W, Parr RG. Development of the Colle-Salvetti Correlation-Energy Formula into a Functional of the Electron Density. 1988. Phys. Rev. B 37:785-789.

Lindner H, Helliger W. Age-dependent deamidation of asparagine residues in proteins. 2001. Experimental Gerontology 36:1551-1563.

Milne GWA, Axenrod T, Fales HM. Chemical Ionization Mass Spectrometry of Complex Molecules. IV. Amino Acids. 1970. J. Am. Chem. Soc. 92:5170-5175.

Moision RM, Armentrout PB. An Experimental and Theoretical Dissection of Sodium Cation/Glycine Interactions. 2002. J. Phys. Chem. A 106:10350-10362.

Moision RM, Armentrout PB. The Special Five-membered Ring of Proline: An Experimental and Theoretical Investigation of Alkali Metal Cation Interactions with Proline and Its Four- and Six-membered Ring Analogues. 2006. J. Phys. Chem. A 110:3933-3946.

Moision RM, Armentrout PB. An Electrospray Ionization Source for Thermochemical Investigation with the Guided Ion Beam Mass Spectrometer. 2007. J. Am. Soc. Mass Spectrom. 18:1124-1134.

Mookherjee A, Armentrout PB. Role of Methylation on the Thermochemistry of Alkali Metal Cation Complexes of Amino Acids: N-Methyl Proline. 2013. Int. J. Mass Spectrom. 345-347:109-119.

Mookherjee A, Armentrout PB. Theoretical Investigation and Reinterpretation of the Decomposition of Lithiated Proline and N-Methyl Proline. 2014. Int. J. Mass Spectrom. 370:16-28.

Mookherjee A, Armentrout PB. Thermodynamics and Reaction Mechanisms for Decomposition of a Simple Protonated Tripeptide, H⁺GAG: a Guided Ion Beam and Computational Study. 2019. J. Am. Soc. Mass Spectrom. 30:1013-1027.

Mookherjee A, Van Stipdonk MJ, Armentrout PB. Thermodynamics and Reaction Mechanisms of Decomposition of the Simplest Protonated Tripeptide, Triglycine: A Guided Ion Beam and Computational Study. 2017. J. Am Soc. Mass Spectrom. 28:739-757.

Muntean F, Armentrout PB. Guided Ion Beam Study of Collision-Induced Dissociation Dynamics: Integral and Differential Cross Sections. 2001. J. Chem. Phys. 115:1213-1228.

Nilsson MR, Driscoll M, Raleigh DP. Low Levels of Asparagine Deamidation Can Have a Dramatic Effect on Aggregation of Amyloidogenic Peptides: Implications for the Study of Amyloid Formation. 2002. Protein Sci. 11:342-349.

O'Brien JT, Prell JS, Steill JD, Oomens J, Williams ER. Interactions of Mono- and Divalent Metal Ions with Aspartic and Glutamic Acid Investigated with IR Photodissociation Spectroscopy and Theory. 2008. J. Phys. Chem. A 112:10823-10830.

O'Hair RAJ, Broughton PS, Styles ML, Frink BT, Hadad CM. The Fragmentation Pathways of Protonated Glycine: A Computational Study. 2000. J. Am. Soc. Mass Spectrom. 11:687-696.

O'Hair RAJ, Styles ML, Reid GE. Role of the sulfhydryl group on the gas phase fragmentation reactions of protonated cysteine and cysteine containing peptides. 1998. J. Am. Soc. Mass Spectrom. 9:1275-1284.

Oomens J, Kempkes LJM, Geurts TPJ, van Dijk L, Martens J, Berden G, Armentrout PB. Water Loss from Protonated XxxSer and XxxThr Dipeptides Gives Oxazoline—Not Oxazolone—Product Ions. 2020. J. Am. Soc. Mass Spectrom. 31:2111-2123.

Paizs B, Csonka I, Lendvay G, Suhai S. Proton mobility in protonated glycylglycine and N-formylglycylglycinamide: a combined quantum chemical and RKKM study. 2001. Rapid Commun. Mass Spectrom. 15:637-650.

Paizs B, Suhai S. Combined Quantum Chemical and RRKM Modeling of the Main Fragmentation Pathways of Protonated GGG. I. Cis-Trans Isomerization around Protonated Amide Bonds. 2001a. Rapid Commun. Mass Spectrom. 15:2307-2323.

Paizs B, Suhai S. Theoretical Study of the Main Fragmentation Pathways for Protonated Glycylglycine. 2001b. Rapid Commun. Mass Spectrom. 15:651-663.

Paizs B, Suhai S. Combined Quantum Chemical and RRKM Modeling of the Main Fragmentation Pathways of Protonated GGG. II. Formation of b₂, y₁, and y₂ Ions. 2002. Rapid Commun. Mass Spectrom. 16:375-389.

Pingitore F, Polce MJ, Wang P, Wesdemiotis C, Paizs B. Intramolecular Condensation Reactions in Protonated Dipeptides: Carbon Monoxide, Water, and Ammonia Losses in Competition. 2004. J. Am. Soc. Mass Spectrom. 15:1025-1038.

Polfer NC, Oomens J, Dunbar RC. IRMPD Spectroscopy of Metal-Ion/Tryptophan Complexes. 2006. Phys. Chem. Phys. 8:2744-2751.

Polfer NC, Paizs B, Snoek LC, Compagnon I, Suhai S, Meijer G, von Helden G, Oomens J. Infrared Fingerprint Spectroscopy and Theoretical Studies of Potassium Ion Tagged Amino Acids and Peptides in the Gas Phase. 2005. J. Am. Chem. Soc. 127:8571-8579.

Reid GE, Simpson RJ, O'Hair RAJ. Probing the fragmentation reactions of protonated glycine oligomers via multistage mass spectrometry and gas phase ion molecule hydrogen/deuterium exchange. 1999. Int. J. Mass Spectrom. 190/191:209-230.

Robinson NE, Robinson AB. Deamidation of Human Proteins. 2001. Proc. Natl. Acad. Sci. 98:12409-12413.

Robinson NE, Robinson AB. 2004. Molecular Clocks: Deamidation of Asparaginyl and Glutaminyl Residues in Peptides and Proteins. Cave Junction, OR: Althouse Press.

Robinson PJ, Holbrook KA. 1972. Unimolecular Reactions. New York: Wiley Interscience.

Rodgers MT, Armentrout PB. Statistical Modeling of Competitive Threshold Collision-Induced Dissociation. 1998. J. Chem. Phys. 109:1787-1800.

Rodgers MT, Armentrout PB. Cationic Noncovalent Interactions: Energetics and Periodic Trends. 2016a. Chem. Rev. 116:5642–5687

Rodgers MT, Armentrout PB. 2016b. Discriminating Properties of Metal Alkali Ions towards the Constituents of Proteins and Nucleic Acids. Conclusions from Gas-Phase and Theoretical Studies. In: Sigel A, Sigel H, Sigel RKO, Editors. Metal Ions in Life Sciences. Volume 16: The Alkali Metal Ions: Their Role for Life. Cham, Switzerland: Springer. p 103-131.

Rodgers MT, Armentrout PB, Oomens J, Steill JD. Infrared Multiphoton Dissociation Spectroscopy of Cationized Threonine: Effects of Alkali-Metal Cation Size on Gas-Phase Conformation. 2008. J. Phys. Chem. A 112:2258-2267.

Rodgers MT, Ervin KM, Armentrout PB. Statistical Modeling of Collision-Induced Dissociation Thresholds. 1997. J. Chem. Phys. 106:4499-4508.

Rodriquez CF, Cunje A, Shoeib T, Chu IK, Hopkinson AC, Siu KWM. Proton Migration and Tautomerism in Protonated Triglycine. 2001. J. Am. Chem. Soc. 123:3006-3012.

Rogalewicz F, Hoppilliard Y, Ohanessian G. Fragmentation Mechanisms of α -Amino Acids Protonated Under Electrospray Ionization: A Collisional Activation and Ab Initio Theoretical Study. 2000. Int. J. Mass Spectrom. 195/196:565-569.

Ruan C, Rodgers MT. Cation- π Interactions: Structures and Energetics of Complexation of Na⁺ and K⁺ with the Aromatic Amino Acids, Phenylalanine, Tyrosine and Tryptophan. 2004. J. Am. Chem. Soc. 126:14600-14610.

Schlegel HB. Optimization of equilibrium geometries and transition structures. 1982. J. Comput. Chem. 3:214-218.

Shoeib T, Zhao J, Aribi HE, Hopkinson AC, Siu KWM. Dissociations of Complexes Between Monovalent Metal Ions and Aromatic Amino Acid or Histidine. 2013. J. Am. Soc. Mass. Spectrom. 24:38-48.

Stein SE, Rabinovich BS. On the Use of Exact State Counting Methods in RRKM Rate Calculations. 1977. Chem. Phys. Lett. 49:183-188.

Stein SE, Rabinovitch BS. Accurate Evaluation of Internal Energy Level Sums and Densities Including Anharmonic Oscillators and Hindered Rotors. 1973. J. Chem. Phys. 58:2438-2445.

Sztáray J, Memboeuf A, Drahos L, Vékey K. Leucine enkephalin—A mass spectrometry standard. 2011. Mass Spectrom. Rev. 30:298-320.

Teloy E, Gerlich D. Integral Cross Sections for Ion-Molecule Reactions. 1. The Guided Beam Technique. 1974. Chem. Phys. 4:417-427.

Tsang CW, Harrison AG. Chemical Ionization of Amino Acids. 1976. J. Am. Chem. Soc. 98:1301-1308.

Tsang Y, Wong CCL, Wong CHS, Cheng JMK, Ma NL, Tsang CW. Proton and Potassium Affinities of Aliphatic and N-Methylated Aliphatic α-Amino Acids: Effect of Alkyl Chain Length on Relative Stabilities of K⁺ Bound Zwitterionic Complexes. 2012. Int. J. Mass Spectrom. 316-318:273-283.

Tu Y-P, Harrison AG. The b1 ion derived from methionine is a stable species. 1998. Rapid Commun. Mass Spectrom. 12:849-851.

Uggerud E. The unimolecular chemistry of protonated glycine and the proton affinity of glycine: a computational model. 1997. Theor. Chem. Acc. 97:313-316.

Verkerk UH, Siu C-K, Steill JD, El Aribi H, Zhao J, Rodriguez CF, Oomens J, Hopkinson AC, Siu KWM. a₂ Ion Derived from Triglycine: An N₁-protonated 4-Imidazolidinone. 2010. J. Phys. Chem. Lett. 1:868-872.

Waage EV, Rabinovitch BS. Centrifugal Effects in Reaction Rate Theory. 1970. Chem. Rev. 70:377-387.

Wang P, Ohanessian G, Wesdemiotis C. The Sodium Ion Affinities of Asparagine, Glutamine, Histidine and Arginine. 2008. Int. J. Mass Spectrom. 269:34-45.

Wang P, Wesdemiotis C, Kapota C, Ohanessian G. The Sodium Ion Affinities of Simple Di-, Tri-, and Tetrapeptide. 2007. J. Am. Soc. Mass Spectrom. 18:541-552.

Wu R, McMahon TB. Infrared Multiple Photon Dissociation Spectroscopy as Structural Confirmation for GlyGlyGlyH⁺ and AlaAlaAlaH⁺ in the Gas Phase. Evidence for Amide Oxygen as the Protonation Site. 2007. J. Am. Chem. Soc. 129:11312-11313.

Wysocki VH, Tsaprailis G, Smith LL, Breci LA. Mobile and Localized Protons: A Framework for Understanding Peptide Dissociation. 2000. J. Mass Spectrom. 35:1399–1406.

Yalcin T, Harrison AG. Ion chemistry of protonated lysine derivatives. 1996. J. Mass Spectrom. 31:1237-1243.

Ye SJ, Armentrout PB. Absolute Thermodynamic Measurements of Alkali Metal Cation Interactions with a Simple Dipeptide and Tripeptide. 2008a. J. Phys. Chem. A 112:3587-3596.

Ye SJ, Armentrout PB. An Experimental and Theoretical Investigation of the Decomposition of Lithiated Hydroxyl Side Chain Amino Acids. 2008b. J. Phys. Chem. B 112:10303-10313.

Ye SJ, Clark AA, Armentrout PB. An Experimental and Theoretical Investigation of Alkali Metal Cation Interactions with Hydroxyl Side Chain Amino Acids. 2008. J. Phys. Chem. B 112:10291-10302.

Zhang P, Chan W, Ang IL, Wei R, Lam MMT, Lei KMK, Poon TCW. Revisiting Fragmentation Reactions of Protonated α-Amino Acids by High-Resolution Electrospray Ionization Tandem Mass Spectrometry with Collision-Induced Dissociation. 2019. Scientific Reports 9:6453.

Zlokovic BV. New therapeutic targets in the neurovascular pathway in Alzheimer's disease. 2008. Neurotherapeutics: the journal of the American Society for Experimental NeuroTherapeutics 5:409-414.